
1 NAQPMS-PDAF v2.0: A Novel Hybrid Nonlinear Data Assimilation 2 System for Improved Simulation of PM_{2.5} Chemical Components

3 Hongyi Li^{1, 3}, Ting Yang¹, Lars Nerger⁴, Dawei Zhang², Di Zhang², Guigang Tang², Haibo Wang¹, Yele
4 Sun^{1, 3}, Pingqing Fu⁵, Hang Su^{1, 6}, Zifa Wang^{1, 3}

5 ¹State Key Laboratory of Atmospheric Boundary Layer Physics and Atmospheric Chemistry (LAPC), Institute of Atmospheric
6 Physics, Chinese Academy of Sciences, Beijing 100029, China.

7 ²China National Environmental Monitoring Centre, Beijing, China

8 ³College of Earth and Planetary Sciences, University of Chinese Academy of Sciences, Beijing 100049, China

9 ⁴Alfred Wegener Institute, Helmholtz Center for Polar und Marine Research, Bremerhaven, Germany

10 ⁵Institute of Surface-Earth System Science, School of Earth System Science, Tianjin University, Tianjin 300072, China

11 ⁶Max Planck Institute for Chemistry, Mainz, Germany

12 *Correspondence to:* Ting Yang (tingyang@mail.iap.ac.cn)

13 **Abstract.** ~~Identifying PM_{2.5}, a complex mixture with diverse~~ chemical components, ~~exerts significant impacts on the~~
14 ~~environment, is crucial for formulating emission strategies, estimating radiative forcing, and assessing~~ human health, ~~and~~
15 ~~climate change effects.~~ However, ~~precisely~~ accurately describing spatiotemporal variations of PM_{2.5} chemical components
16 remains a ~~difficulty~~ challenge. In our earlier work, we developed an aerosol extinction coefficient data assimilation (DA) system
17 (NAQPMS-PDAF v1.0) ~~that is~~ suboptimal for chemical components. This paper introduces a novel hybrid nonlinear chemical
18 DA system (NAQPMS-PDAF v2.0) to accurately interpret key chemical components (SO₄²⁻, NO₃⁻, NH₄⁺, OC, and EC).
19 NAQPMS-PDAF v2.0 improves upon v1.0 by effectively ~~handling~~ handling and balancing stability and nonlinearity in chemical
20 DA, which is achieved by incorporating the non-Gaussian-distribution ensemble perturbation and hybrid Localized Kalman-
21 Nonlinear Ensemble Transform Filter with an adaptive forgetting factor for the first time. The dependence tests demonstrate
22 that NAQPMS-PDAF v2.0 provides excellent DA results with a minimal ensemble size of 10, surpassing previous reports and
23 v1.0. A one-month DA experiment shows that the analysis field generated by NAQPMS-PDAF v2.0 is in good agreement with
24 observations, especially in reducing the underestimation of NH₄⁺ and NO₃⁻ and the overestimation of SO₄²⁻, OC, and EC. In
25 particular, the CORR values for NO₃⁻, OC, and EC are above 0.96, and R² values are above 0.93. NAQPMS-PDAF v2.0 also
26 demonstrates superior spatiotemporal interpretation, with most DA sites showing improvements of over 50%-200% in CORR
27 and over 50%-90% in RMSE for the five chemical components. Compared to the poor performance in global reanalysis dataset
28 (CORR: 0.42-0.55, RMSE: 4.51-12.27 μg/m³) and NAQPMS-PDAF v1.0 (CORR: 0.35-0.98, RMSE: 2.46-15.50 μg/m³),
29 NAQPMS-PDAF v2.0 has the highest CORR of 0.86-0.99 and the lowest RMSE of 0.14-3.18 μg/m³. The uncertainties in
30 ensemble DA are also examined, further highlighting the potential of NAQPMS-PDAF v2.0 for advancing aerosol chemical
31 component studies.

32 1 Introduction

33 PM_{2.5} is a complex mixture of various chemical fractions, mainly including sulfate (SO₄²⁻), nitrate (NO₃⁻), ammonium (NH₄⁺),
34 organic carbon (OC), and elemental carbon (EC), ~~which diversely~~. These chemical components exert diverse influences on
35 the atmospheric environment (Khanna et al., 2018), human health (Bell et al., 2007; Schlesinger, 2007; Li et al., 2022a; Alves
36 et al., 2023), and climate change (Schult et al., 1997; Park et al., 2014; Wilcox et al., 2016). However, current detection
37 technologies, such as ~~field~~direct observation ~~with in-situ~~by sampling and chemical analysis (Zhang et al., 2015; Ming et al.,
38 2017), ground-based remote-sensing inversion (Nishizawa et al., 2008; Nishizawa et al., 2011; Nishizawa et al., 2017), and
39 observation-based machine learning (Lin et al., 2022; Su Lee et al., 2023; Li et al., 2025), are insufficient in interpreting
40 spatiotemporally continuous information of PM_{2.5} chemical components due to the ~~spatiotemporal discontinuity and~~-limited
41 ~~chemical species~~number of observation sites or platforms. Although atmospheric chemistry transport models (CTMs) (Wang
42 et al., 2014; Wang et al., 2015; Jia et al., 2017; Yang et al., 2019; Li et al., 2020; Lv et al., 2020) are ~~commonly~~widely used to
43 characterize the spatiotemporal distribution of multiple chemical species, CTMs are ~~associated with~~constrained by
44 uncertainties in initial-boundary conditions, physiochemical mechanisms, emission inventories, and meteorological fields (Sax
45 and Isakov, 2003; Mallet and Sportisse, 2006; Rodriguez et al., 2007; Chang et al., 2015; Miao et al., 2020; Xie et al., 2022),
46 resulting in ~~biases relative to real situation~~notable discrepancies between the model simulations and accurate observations.

47
48 Data assimilation (DA) offers a solution to integrate the multi-source observations, CTMs, and their uncertainties effectively
49 to enhance the simulation and forecasting capabilities of CTMs. Variational methods (3D-Var/4D-Var) (Talagrand and Courtier,
50 1987), Ensemble Kalman Filter (EnKF) (Evensen, 1994; Evensen, 2003), EnKF-variants (EnKFs) (Bishop et al., 2001; Tippett
51 et al., 2003; Hunt et al., 2007; Nerger et al., 2012), and hybrid EnKF-Var methods (Hamill and Snyder, 2000; Schwartz et al.,
52 2014) are most widely applied in DA. However, variational methods have a flow-independent Background Error Covariance
53 (BEC) with the assumption of isotropic, static, and uniform characteristics, and they need to develop the tangent linear adjoint
54 model, which is difficult to practice for complex models. Although EnKFs and hybrid EnKF-Var methods have a flow-
55 dependent BEC, they are sensitive to inadequate ensemble sampling and have high computational costs. Importantly, these
56 methods cannot address model nonlinearity and non-Gaussian error distribution, yielding suboptimal results for DA in highly
57 nonlinear CTMs.

58
59 Currently, nonlinear filters, such as Particle Filter (PF) (Gordon et al., 1993) and Nonlinear Ensemble Transform Filter (NETF)
60 (Tödter and Ahrens, 2015), have been proposed to approximate the complete posterior probability distribution of model states
61 and provide a better representation of non-Gaussian information based on Monte Carlo random sampling and Bayesian theory.

62 However, PF is unstable and susceptible to filter degeneration compared to EnKFs. In a recent study, Nerger (2022) proposed
63 the hybrid Kalman-Nonlinear Ensemble Transform Filter (KNETF) to achieve excellent DA performance in the Lorenz-63 and
64 Lorenz-96 model with a smaller ensemble size, which combines the stability of EnKFs and the nonlinearity of NETF (Nerger,
65 2022). However, to the author's knowledge, this algorithm has not been applied to the chemical DA of CTMs.

66
67 Studies on chemical DA involve the assimilation of aerosol optical properties, such as aerosol optical depth (AOD) and
68 extinction coefficient (EXT), and the particulate matters (PMs), such as the mass concentrations of PM_{2.5} and PM₁₀. The
69 commonly AOD observations for DA include OMI-AOD (Ali et al., 2013), MODIS-AOD (Zhang et al., 2008; Huneeus et al.,
70 2012; Huneeus et al., 2013; Rubin and Collins, 2014; Lynch et al., 2016; Werner et al., 2019; Kumar et al., 2020), AERONET-
71 AOD (Schutgens et al., 2010; Li et al., 2016), Sun-Sky Photometer-Multiband AOD (Chang et al., 2021), GOCI-AOD (Saide
72 et al., 2014; Luo et al., 2020; Kim et al., 2021), and Fengyun/Himawari8-AOD (Bao et al., 2019; Jin et al., 2019; Xia et al.,
73 2019; Xia et al., 2020). These studies indicated that AOD observations can enhance the accuracy of aerosol simulation and
74 forecast. Compared to AOD, EXT DA effectively improves the interpretation of aerosol vertical distribution (Zhang et al.,
75 2014; Cheng et al., 2019; Wang et al., 2022). Additionally, the simultaneous DA of aerosol optical properties and PMs is widely
76 applied in aerosol studies (Tang et al., 2015; Chai et al., 2017). According to our literature review (Yang et al., 2023), there is
77 currently no DA study on aerosol chemical components due to the limited DA influence of PMs and AOD on chemical
78 compositions (Chang et al., 2021) and the limited chemical observations with an extensive spatial range. Moreover, the aerosol
79 chemical components exhibit nonlinearity and a non-Gaussian distribution (Ha, 2022), while current main-stream algorithms,
80 such as variational methods or EnKFs, are suboptimal for chemical component DA.

81
82 In our previous work, we developed an aerosol vertical DA system (NAQPMS-PDAF v1.0) based on EnKFs to improve the
83 simulation of the extinction coefficient vertical profile (Wang et al., 2022). In this study, we present a novel hybrid nonlinear
84 DA system (NAQPMS-PDAF v2.0) towards various PM_{2.5} chemical components through online integration of Parallel Data
85 Assimilation Framework (PDAF, version 2.1, released on February 21st, 2023), Observation Module Infrastructure (OMI) and
86 Nested Air Quality Prediction Model System (NAQPMS). We collected 1-month hourly surface observations of five PM_{2.5}
87 chemical components (NH₄⁺, SO₄²⁻, NO₃⁻, OC, and EC) over Northern China and surrounding areas. We utilized the hybrid
88 Localized Kalman-Nonlinear Ensemble Transform Filter (LKNETF) to generate a high-resolution and high-accuracy
89 reanalysis dataset of PM_{2.5} chemical components for the first time. Notably, the ensemble members in NAQPMS-PDAF v2.0
90 are generated by perturbing emission species based on their uncertainties and non-Gaussian distribution assumption. Section
91 2 briefly introduces NAQPMS and PDAF v2.1 with OMI, respectively, and details the development of NAQPMS-PDAF v2.0,

92 including system structure, configuration, ensemble generation, and LKNETF algorithm. The data used in this study and
93 experimental settings are also described in Section 2. Section 3 presents the DA results, including ~~evaluating an evaluation of~~
94 dependencies, performance, and external comparisons. ~~Besides, Section 3 discusses, as well as a discussion of~~ the ensemble
95 DA uncertainty. Section 4 summarizes the conclusions and outlook.

96 **2 Method and data**

97 **2.1 NAQPMS**

98 The Nested Air Quality Prediction Modeling System (NAQPMS), developed by the Institute of Atmospheric Physics
99 (IAP), Chinese Academy of Sciences (CAS), is used to provide background fields ~~of key aerosol chemical components in this~~
100 ~~study.~~ ~~for key aerosol chemical components in this study.~~ NAQPMS is a multi-scale gridded 3-dimensional Eulerian chemical
101 ~~transport model based on continuity equations. The nested grids in the horizontal direction enable data exchange between~~
102 ~~different domains. Applying terrain-following coordinates in the vertical direction mitigates numerical calculation errors to~~
103 ~~enhance model accuracy. The NAQPMS comprises an input section, a numerical computation section, and an output section.~~
104 ~~The input section incorporates static terrain data, emission inventories, meteorological fields, and initial-boundary conditions.~~
105 ~~The numerical computation section performs multiple physicochemical process calculations, including the advection process,~~
106 ~~eddy diffusion, dry deposition, wet scavenging, gas-phase chemistry, aqueous chemistry, aerosol physicochemical processes~~
107 ~~(including heterogeneous reactions at the aerosol surface), and other processes. The schemes and features of the~~
108 ~~physicochemical processes are summarized in Table S1. The output section is responsible for model post-processing, data~~
109 ~~diagnostics, and source identification.~~

11 NAQPMS is capable of characterizing the three-dimensional spatiotemporal distribution of various atmospheric compositions
12 at global and regional scales ~~through multiple physicochemical processes (shown in Table S1)~~ and has been widely used in
13 atmospheric pollution and chemistry research, such as O₃ pollution; (Wang et al., 2001), haze episodes (Wang et al., 2014; Du
14 et al., 2021), regional transport (Wang et al., 2017; Wang et al., 2019), source identification (Li et al., 2022b), air quality
15 simulation at global scale (Ye et al., 2021) and at urban-street scale (Wang et al., 2023), and acid deposition (Ge et al., 2014).

16 **2.2 PDAF v2.1 with OMI**

17 The Parallel Data Assimilation Framework (PDAF, <https://pdaf.awi.de/trac/wiki>) is an open-source and high-expandability
18 software developed by the Alfred Wegener Institute (AWI) in Germany to integrate observations, numerical models, and
19 assimilation systems for DA tasks, widely applied in meteorology, oceanography, land surface and atmospheric chemistry

20 (Kurtz et al., 2016; Nerger et al., 2020; Mingari et al., 2022; Strebel et al., 2022; Wang et al., 2022; Yu et al., 2022). The initial
21 version of PDAF (PDAF v1.0) was released in 2004. It has undergone continuous improvements and updates, with major
22 updates including the introduction of Ensemble Transform Kalman Filter (ETKF) and its localized variant (LETKF) in version
23 1.6, the implementation of PDAF-OMI (Observation Module Infrastructure) in version 1.16, the integration of 3D-Var methods
24 in version 2.0, and the incorporation of the hybrid KNETF and its localized variant (LKNETF) for the first time in version 2.1,
25 which was released in 2023 to handle the complex DA situations, such as the nonlinearity of system and non-Gaussian error
26 distribution of model state. Notably, the version of PDAF coupled in NAQPMS-PDAF v1.0 is PDAF v1.15 (released in 2019),
27 implying that NAQPMS-PDAF v1.0 has more limited applicability and functionality. In this work, the PDAF v2.1 is coupled
28 in NAQPMS-PDAF v2.0.

29
30 PDAF has ~~two modes, namely~~ offline and online ~~modemodes~~. For the offline mode, PDAF and the model perform separately
31 without coupling, ~~which is easy obviating the need to write~~ ~~modify the model~~ code. For the online mode, PDAF is coupled with
32 the model, and model calculation and data assimilation ~~performare performed~~ continuously. Compared to the offline mode,
33 the online coupling has several advantages. Firstly, the initialization ~~process of the~~ PDAF and the model ~~only needs to be~~
34 ~~executed once instead of twice independently~~ ~~is integrated, necessitating a single execution rather than two separate executions~~.
35 Secondly, the model integration result can be directly passed to PDAF for data assimilation. Additionally, the assimilation
36 result of PDAF can be directly passed to the model for the next model integration. ~~This~~ The online mode eliminates the need
37 for intermediate steps and improves efficiency. Thirdly, the online mode is controlled by a main program, which allows for
38 efficient use of several processors in the high-performance computing cluster. Conversely, in the offline mode, the PDAF and
39 the model are managed by distinct programs, often with ~~a reduced number of~~ ~~fewer~~ processors available for each program.
40 Therefore, the online-mode PDAF is used in this study.

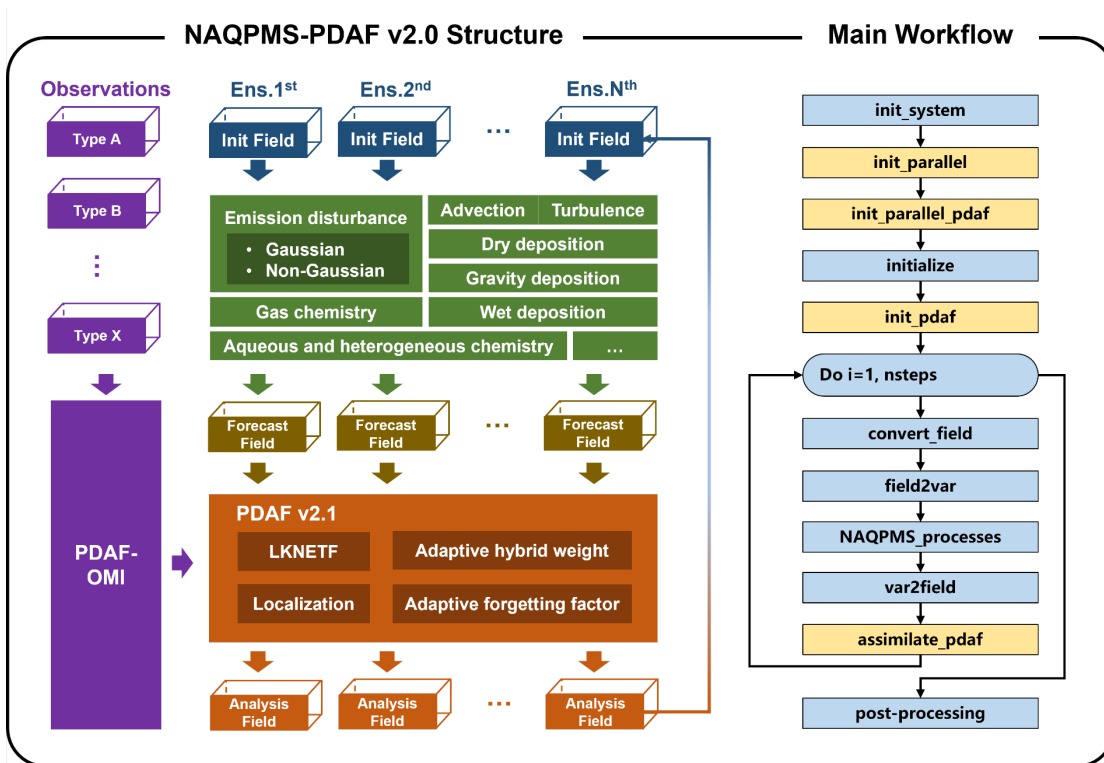
41
42 PDAF-OMI, an extension of PDAF, provides I/O interfaces for multi-type observations, simplifying user observation handling
43 by offering generic PDAF-OMI core routines and independent user-supplied routines for each observational type. The user-
44 supplied routines, namely *init_dim_obs/init_dim_obs_l*, *obs_op*, and *localize_covar*, are responsible for reading and writing
45 multi-type observations, applying corresponding observation operators, and performing covariance localization, respectively.
46 The modules for all observation types are integrated into the *callback_obs_pdafomi*, allowing free combinations between
47 different observation types without interference and facilitating the collaborative DA for various aerosol chemical components.
48 PDAF-OMI was not applied in NAQPMS-PDAF v1.0. Consequently, NAQPMS-PDAF v1.0 cannot switch between different
49 observational type combinations, and users need to define complete routines for each observation type for the DA process,

50 resulting in more tedious code writing and higher computational costs in NAQPMS-PDAF v1.0.

51 2.3 NAQPMS-PDAF v2.0

52 2.3.1 Structure of NAQPMS-PDAF v2.0

53 Figure 1 illustrates the structure (left portion) and main workflow (right portion) of NAQPMS-PDAF v2.0. The
54 ~~observational~~As described in the left portion of Fig. 1, the observation part involves the integration of multi-type observations
55 (the purple cuboid patterns) and the utilization of PDAF-OMI. PDAF-OMI enables the simultaneous access and scheduling of
56 multi-type and multi-source ~~data through observations by employing~~ observational indices, ~~which allows for thereby~~
57 facilitating flexible ~~combination combinations~~ of observations. The ensemble initial fields (the deep blue cuboid patterns) are
58 crucial inputs for the numerical simulation of NAQPMS. The ensemble forecast/background fields (the deep yellow cuboid
59 patterns) are generated by perturbing emission species based on hypothesized distributions (see Sect. 2.3.3) and
60 NAQPMS performing physiochemical calculations in NAQPMS (the green part in Fig. 1) rectangular patterns). Then, chemical
61 DA is performed by a novel hybrid localized nonlinear DA algorithm (LKNETF, see Sect. 2.3.4) with an adaptive hybrid
62 weight and an adaptive forgetting factor to generate analysis/initial fields (the orange cuboid patterns) for the next realization.



63
64 **Figure 1: The structure of NAQPMS-PDAF v2.0**

65 Figure 1: The structure of NAQPMS-PDAF v2.0 (Left: the purple cuboid patterns represent the multi-type observations, the deep
66 blue cuboid patterns represent the initial fields, the deep yellow cuboid patterns represent the forecast or background fields, and the
67 orange cuboid patterns represent the analysis fields. Ens.1st represents the first ensemble member, and Ens.Nth represents the Nth
68 ensemble member. Right: the main workflow in NAQPMS-PDAF v2.0, blue rectangular patterns represent the modules in NAQPMS,

69 and yellow rectangular patterns represent the modules in PDAF).

70 NAQPMS-PDAF v2.0 implements an online coupling between NAQPMS and PDAF v2.1 with OMI, utilizing a level-2
71 parallel computational framework. The description of level-2 parallel implementation was detailed in our previous work (Wang
72 et al., 2022). The online coupling ensures the continuous operation of model forecasts and assimilation analysis at each time
73 step, achieved by directly integrating PDAF routines into the prototype code of NAQPMS (~~In Fig. 1~~ the right ~~part~~ portion of
74 Fig. 1, the blue represents NAQPMS main routines, while the yellow represents PDAF main routines). The level-2 parallel
75 computational framework, which utilizes the Message Passing Interface standard (MPI), facilitates concurrent processing and
76 data exchange among multiple ensemble members and parallel computation among model state matrixes within each ensemble
77 member, enhancing the efficiency of ensemble analysis and numerical model computations. ~~The description of level 2 parallel~~
78 ~~implementation was detailed in our previous work (Wang et al.~~ For instance, the operation of twenty ensemble members
79 necessitates the execution of twenty model tasks, each of which performs integral calculations on a large model grid. Twenty
80 model tasks can be executed simultaneously at twenty computational nodes with sufficient computational resources. Each
81 model task can then perform parallel computation with multiple processors by splitting the large model grid into multiple sub-
82 grids. As illustrated in the right portion of Fig. 1, the ~~2022).~~ The workflow of NAQPMS-PDAF v2.0 is outlined as follows:

83 Step 1. *init_system* module initializes NAQPMS, ~~such as by~~ defining all model state variables, allocating numerical matrixes,
84 configuring parameters, I/O of meteorological fields, and emission input.

85 Step 2. *init_parallel* module initializes MPI (MPI_COMM_WORLD) and model communicator (MPI_COMM_MODEL),
86 their number of processes, and the rank of a process, followed by *init_parallel_pdaf*, which initializes MPI communicators for
87 the model tasks, filter tasks and the coupling between model and filter tasks.

88 Step 3. *initialize* module initializes the target field (such as PM_{2.5} chemical components), such as their spatiotemporal
89 dimensions (longitude, latitude, and time steps) and variable dimensions.

90 Step 4. *init_pdaf* module initializes PDAF variables, such as the local state dimension, global state dimension, and settings for
91 analysis steps.

92 Step 5. Perform the time loop of forecast and analysis. The *convert_field* module is employed to match the matrix storage rule
93 of the target field between NAQPMS and PDAF to ensure compatibility. The *field2var* module collects the analysis field/initial
94 field and establishes a relationship between the initial field/analysis field and sub-variables in NAQPMS. Subsequently, the
95 analysis field values are allocated to the corresponding NAQPMS sub-variables, and then the *NAQPMS_processes* module
96 performs the forecast. After that, the *var2field* module, the inverse of the *field2var* module, assigns the NAQPMS sub-variables
97 to the forecast field/background field. Finally, the *assimilate_pdaf* module assimilates the target field with observations to
98 generate an analysis field for the next iteration.

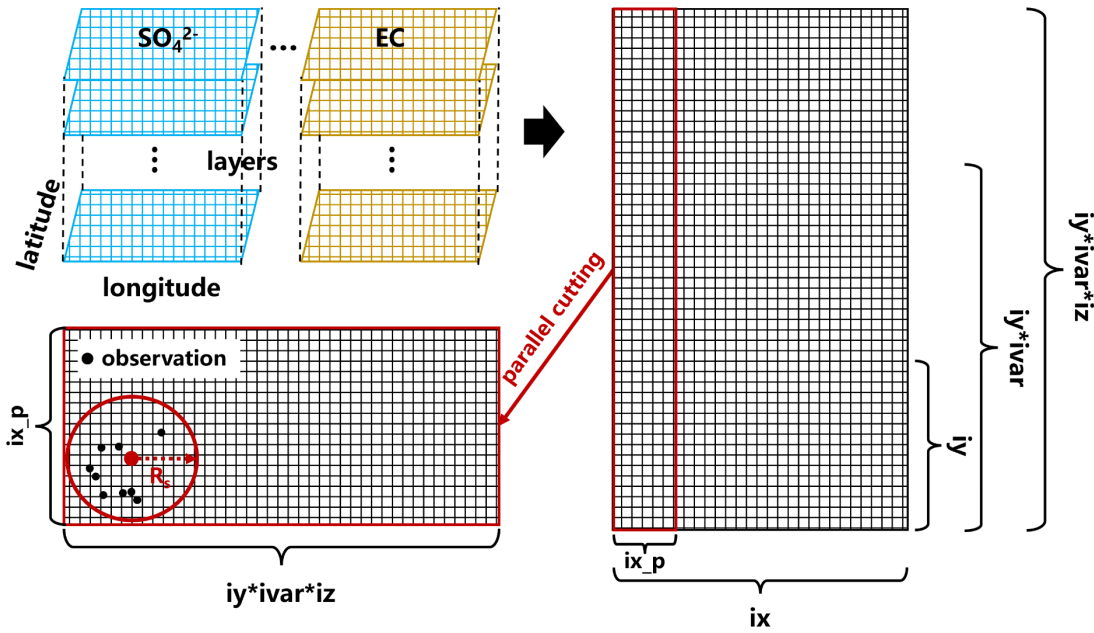
99 Step 6. The post-processing module is responsible for finalizing NAPQMS-PDAF, data analysis, and DA evaluation.

100 2.3.2 ~~Configures~~Configurations

101 The meteorological field for NAQPMS is provided by the Weather Research and Forecasting model version 4.0 (WRFV4.0,
102 <https://www.mmm.ucar.edu/models/wrf>). The initial-boundary conditions for WRF are obtained from NCEP GDAS Final
103 Analysis (<https://rda.ucar.edu/datasets/ds083.3/>), with a horizontal resolution of $0.25^{\circ} \times 0.25^{\circ}$ and the temporal resolution of 6
104 hours, produced by the Global Data Assimilation System (GDAS). The land use data for WRF was updated by USGS's
105 MCD12Q1 v006 in 2019 (<https://lpdaac.usgs.gov/products/mcd12q1v006/>) with 20 categories. Three nested model domains
106 are conducted with the horizontal resolutions of 45 km in the East Asia region (domain1), 15 km in most areas of China except
107 for the western area (domain2), and 5 km in the Northern China region (domain3, target research region). WRF and NAQPMS
108 have 40 vertical layers with 27 layers within 2 km. The parameterization schemes for physical processes in WRF are shown
109 in Table S2. The boundary condition input for NAQPMS is provided by the global chemistry transport Model for Ozone And
110 Related chemical Tracers version 2.4 (MOZART V2.4) (Horowitz et al., 2003). The anthropogenic emissions for NAQPMS
111 are from Tsinghua University's 2016 Multi-resolution Emissions Inventory for China (MEIC, <http://www.meicmodel.org/>)
112 with a spatial resolution of $0.25^{\circ} \times 0.25^{\circ}$, including residential sources, transportation sources, agricultural sources, industrial
113 sources, and power plant sources. The computational platform is the high-performance supercomputer subsystem cluster with
114 320 computation nodes, a total of 12,800 processors, and about 153 TB memory at the Big Data Cloud Service Infrastructure
115 Platform (BDCSIP), which meets the demand for high-performance parallel computing of NAQPMS-PDAF v2.0.

116
117 The model state variables include NH_4^+ , SO_4^{2-} , NO_3^- , OC, EC, Na^+ , Brown carbon, soil $\text{PM}_{2.5}$, soil PM_{10} , sea salt, fine dust,
118 coarse dust, SO_2 , NO_2 and RH. As shown in Fig. 2, the model state has a 4-dimensional (4-D) structure, with longitudinal
119 dimension (ix, 300 grids), latitudinal dimension (iy, 249 grids), variable dimension (ivar, 15), and vertical dimension (iz, 40
120 layers) in that order. The 4-D model state with 15 variables is converted to a 2-D state matrix in PDAF, the number of grids in
121 the horizontal axis direction is ix, and the number of grids in the vertical axis direction is $iy \cdot ivar \cdot iz$. Notably, the 2-D state
122 matrix coordinate index ~~of the 2-D state matrix~~ contains 3-D information for each variable to implement the horizontal and
123 vertical domain localization separately, because the horizontal and vertical resolutions are not uniform. This structure has two
124 advantages. First, the parallel cutting of the horizontal axis enables the local domain to retain the full dimensional information
125 ($ix_p \cdot iy \cdot ivar \cdot iz$, where ix_p is the longitudinal dimension of the local domain). Secondly, the localization in the local domain
126 permits the analysis to execute only ~~executes~~ within a small domain ($ix_p \cdot iy$) when the length of the horizontal localization
127 radius (R_s) is smaller than iy, which effectively ~~reduces~~reducing the influence of spurious correlations between different state
128 variables. In this study, we set the horizontal and vertical domain localization radius to 200 km (40 grids) and 1 layer. Besides,

29 we further implemented the observation localization to consider the influence of distance between analysis grid and
 30 observational grid (see Sect. 2.3.4). To minimize computational complexity, the observation errors were assumed to be spatially
 31 isotropic, with $0.40 \mu\text{g}/\text{m}^3$, $1.00 \mu\text{g}/\text{m}^3$, $0.50 \mu\text{g}/\text{m}^3$, $3.00 \mu\text{g}/\text{m}^3$, and $0.50 \mu\text{g}/\text{m}^3$ for NH_4^+ , SO_4^{2-} , NO_3^- , OC and EC, respectively.



32
 33 **Figure 2: The structure of state variables in NAQPMS-PDAF v2.0.**

34 **2.3.3 Generation of ensemble members**

35 In ensemble DA, ensemble members interpret the uncertainty of the model or system, characterized by BEC, which
 36 significantly impacts the DA performance (Dai et al., 2014). For CTMs, emission input directly influences the chemical
 37 calculation and substantially contributes to the uncertainty. Perturbing emission input can effectively represent the uncertainty
 38 in aerosol emissions and enhance the consistency of ensemble error spread, thereby improving aerosol DA (Huang et al., 2023).
 39 CTMs are nonlinear, and model state errors are non-Gaussian distributions. To obtain non-Gaussian error distributions, we
 40 followed [the Kong et al. \(2021\)'s](#) method to assume that the emission errors are spatially correlated by an isotropic correlation
 41 model with [thea](#) decorrelation length of 150 km and generate perturbation coefficient matrixes with the same Gaussian
 42 distribution as the emission species, which are subsequently transformed into non-Gaussian distribution matrixes through non-
 43 Gaussian process generation v1.2 (<https://github.com/ECheyne/Gaussian-to-nonGaussian/>)(Cheynet, 2024).

44
 45 The target $\text{PM}_{2.5}$ chemical components are NH_4^+ , SO_4^{2-} , NO_3^- , OC, and EC, ~~and the~~ The perturbed emission species
 46 ~~correspondingly that can directly or indirectly affect the component concentration calculations~~ include SO_2 , NO_x , VOCs, NH_3 ,
 47 CO, PM_{10} , $\text{PM}_{2.5}$, EC, and OC, with the corresponding uncertainties (δ) listed in Table 1. As shown in Eq. (1), the original
 48 emission input matrix (E_p) is multiplied by the corresponding perturbation coefficient matrix (θ_i) to generate the perturbed

emission input matrix (E_i) for each emission species. The calculation of the perturbation coefficient matrix (θ_i) is followed by Eq. (2)-(3). Firstly, N two-dimensional pseudorandom perturbation fields (P_i) are created using Evensen's method (Evensen, 1994). The uncertainties (δ) of the emission species are incorporated into the two-dimensional pseudorandom perturbation fields (P_i) to obtain the final perturbation coefficient matrixes (θ_i). Finally, the Gaussian-distribution perturbation coefficient matrixes (θ_i) were transformed into non-Gaussian distribution coefficient matrixes with a given target skewness (set to 1) and kurtosis (set to 6) by non-Gaussian process generation v1.2, which employs the Moment Based Hermite Transformation Model and a cubic transformation.

Table 1: The uncertainties of emission species in NAQPMS-PDAF v2.0

Species	SO ₂	NO _x	VOC _s	NH ₃	CO	PM ₁₀	PM _{2.5}	EC	OC
Uncertainty δ	2.00	0.31	0.68	0.53	0.70	1.32	1.30	2.08	2.58

$$E_i = E_p \times \theta_i, i = 1, 2, \dots, N, \quad (1)$$

$$\ln \theta_{oi} = \left(\frac{P_i - \frac{1}{N} \times \sum_{i=1}^N P_i}{\sqrt{\frac{1}{N} \times \sum_{i=1}^N (P_i - \frac{1}{N} \times \sum_{i=1}^N P_i)^2}} - \frac{1}{2} \times \ln(1 + \delta^2) \right) \times \sqrt{\ln(1 + \delta^2)}, \quad (2)$$

$$\theta_i = \frac{(\theta_{oi} - \frac{1}{N} \times \sum_{i=1}^N \theta_{oi})}{\sqrt{\frac{1}{N} \times \sum_{i=1}^N (\theta_{oi} - \frac{1}{N} \times \sum_{i=1}^N \theta_{oi})^2}} \times \left(\frac{1}{N} \times \sum_{i=1}^N \theta_{oi} \right) \times \delta + \frac{1}{N} \times \sum_{i=1}^N \theta_{oi}, \quad (3)$$

Notably, all matrix operations involved are Schur ~~Product~~Products. Where E_i denotes the i^{th} ensemble perturbed emission input matrix, E_p ~~denotes~~indicates the original unperturbed emission input matrix and θ_i represents the i^{th} ensemble perturbation coefficient matrix. θ_{oi} is the i^{th} ensemble original perturbation coefficient matrix, which is obtained by mathematical transformation of the i^{th} ensemble pseudorandom perturbation matrix P_i , including standardization, scaling by uncertainty (δ), and logarithm.

2.3.4 Hybrid nonlinear DA algorithm with adaptive forgetting factor

To thoroughly integrate the stability of EnKFs with the nonlinearity of nonlinear filters and be ideal for the nonlinear and non-Gaussian-distribution situations, the hybrid LKNETF is used in this study. This section reviews the algorithms of LETKF, LNETF, and their combination (LKNETF).

ETKF, a deterministic filter in EnKFs, efficiently obtains analysis samples using a transformation matrix and the square root of the forecast error covariance (Bishop et al., 2001). In contrast to stochastic filters in EnKFs, ETKF prevents underestimation of the analysis error covariance resulting from the random observation perturbations. And it is particularly applicable in situations with small ensemble sizes (Lawson and Hansen, 2004). The realization of ETKF can be divided into the forecast and analysis steps.

76 In the forecast step, the forecast state vector (\mathbf{x}_t^f) at t is generated by numerical model (\mathbf{M}) integration of the analysis state
 77 vector (\mathbf{x}_{t-1}^a) at t-1. The forecast error covariance matrix (\mathbf{P}_t^f) can be calculated by the perturbation of the forecast ensemble
 78 ($\mathbf{X}_t^{f'}$).

$$79 \quad \mathbf{x}_t^f = \mathbf{M}(\mathbf{x}_{t-1}^a), \mathbf{X}_t^f = [\mathbf{x}_{1t}^f, \mathbf{x}_{2t}^f, \dots, \mathbf{x}_{Kt}^f] , \quad (4)$$

$$80 \quad \mathbf{P}_t^f = \mathbf{X}_t^{f'} \mathbf{X}_t^{f'^T} , \quad (5)$$

81 Where \mathbf{X}_t^f is the forecast ensemble at t, and K is the number of ensemble members. $\mathbf{X}_t^{f'}$ is the perturbation of the forecast
 82 ensemble at t, calculated by \mathbf{X}_t^f and the forecast ensemble mean $\overline{\mathbf{X}}_t^f$ at t.

83
 84 In the analysis step, the forecast error covariance matrix (\mathbf{P}_t^f) at t is transformed to the analysis error covariance matrix (\mathbf{P}_t^a) at
 85 t by a transform matrix (\mathbf{T}).

$$86 \quad \mathbf{P}_t^a = \mathbf{X}_t^{f'} \mathbf{T} \mathbf{X}_t^{f'^T} , \quad (6)$$

87 The transform matrix (\mathbf{T}) is defined as follows and can be decomposed to a left singular vector matrix (\mathbf{U}), a singular value
 88 matrix (\mathbf{S}), and a right singular vector matrix (\mathbf{V}) through the singular value decomposition.

$$89 \quad \mathbf{T}^{-1} = \rho_{adaptive} (K - 1) \mathbf{I} + (\mathbf{H} \mathbf{X}_t^{f'})^T (\mathbf{L} \cdot \mathbf{R}^{-1}) \mathbf{H} \mathbf{X}_t^{f'} = \mathbf{U} \mathbf{S} \mathbf{V} , \quad (7)$$

$$90 \quad \rho_{adaptive} = \frac{\sigma_{ens}^2}{\sigma_{resid}^2 - \sigma_{obs}^2} , \quad (8)$$

91 Where $\rho_{adaptive}$ is an adaptive forgetting factor, used for the inflation of error covariance estimation (the initial $\rho_{adaptive}$ is
 92 set to 0.9 in this study). σ_{ens}^2 is the mean ensemble variance, σ_{resid}^2 is mean of observation-minus-forecast residual, σ_{obs}^2 is
 93 mean observation variance. \mathbf{I} is the identity matrix. \mathbf{H} is the observation operator. \mathbf{L} is the localization matrix, a weight
 94 matrix calculated by the 5th-order polynomial (Nerger, 2015), implemented in LETKF for observation localization analysis to
 95 avoid observational spurious correlation and filter divergence effectively (Hunt et al., 2007). \mathbf{R} is the observation error
 96 covariance matrix.

97
 98 The analysis state vector (\mathbf{x}_t^a) at t is calculated by the forecast state vector (\mathbf{x}_t^f) at t, the perturbation of the forecast ensemble
 99 ($\mathbf{X}_t^{f'}$) at t and a weight vector (\mathbf{w}).

$$00 \quad \mathbf{x}_t^a = \mathbf{x}_t^f + \mathbf{X}_t^{f'} \mathbf{w} , \quad (9)$$

01 The weight vector (\mathbf{w}) is given by the following equation.

$$02 \quad \mathbf{w} = \mathbf{T} (\mathbf{H} \mathbf{X}_t^{f'})^T (\mathbf{L} \cdot \mathbf{R}^{-1}) (\mathbf{y} - \mathbf{H} \mathbf{x}_t^f) , \quad (10)$$

03 Where \mathbf{y} is observations.

04

05 The analysis ensemble (\mathbf{X}_t^a) at t can be obtained by forecast ensemble mean ($\overline{\mathbf{X}}_t^f$) at t , the perturbation of the forecast ensemble
06 ($\mathbf{X}_t^{f'}$) at t and a transform matrix (\mathbf{C}) represented by the symmetric square root of \mathbf{T} .

$$07 \quad \mathbf{X}_t^a = \overline{\mathbf{X}}_t^f + \sqrt{K-1} \mathbf{X}_t^{f'} \mathbf{C} \quad , \quad (11)$$

08 The transform matrix (\mathbf{C}) is calculated as follows.

$$09 \quad \mathbf{C} = \mathbf{U} \mathbf{S}^{-1/2} \mathbf{U}^T \quad , \quad (12)$$

10 NETF is a 2nd-order exact ensemble square root filter effectively applied to the nonlinear and non-Gaussian DA (Tödter and
11 Ahrens, 2015). Like PF, NETF indirectly updates the model state by using observations to affect the weights of the prior
12 ensemble. However, PF and NETF differ in the sampling method. PF utilizes the Monte Carlo and Bayesian
13 [methods/approaches](#) to calculate particle weights based on observations, which are then used to generate the analysis ensemble
14 by weighting the resampling forecast ensemble. In high-dimensional systems, as the DA progresses, the weight differences of
15 particles increase, with most particles having weights close to 0, leading to filter degeneration. In contrast, NETF generates
16 the analysis ensemble through a deterministic matrix square root transformation of the forecast ensemble, where the mean and
17 covariance matrix of the analysis ensemble match the weighted values in PF (as shown in Eq. (13)-(14)). Due to the similarity
18 between NETF and ETKF, the localization can be implemented in NETF (LNETF) (Tödter et al., 2016).

$$19 \quad \bar{\mathbf{x}}^a = \frac{1}{K} \sum_{i=1}^K \mathbf{x}_i^a = \frac{1}{K} \sum_{i=1}^K w_i \mathbf{x}_i^f \quad , \quad (13)$$

20 Where $\bar{\mathbf{x}}^a$ is the analysis state vector mean, K is the number of ensemble members, \mathbf{x}_i^a is the i^{th} analysis state vector, w_i is
21 the i^{th} particle weight vector in PF, which is calculated by the Bayesian method $w_i = p(\mathbf{y}|\mathbf{x}_i^f)/p(\mathbf{y})$, \mathbf{y} is the observations,
22 \mathbf{x}_i^f is the i^{th} forecast state vector.

$$23 \quad \mathbf{P}^a = \frac{1}{K-1} \sum_{i=1}^K (\mathbf{x}_i^a - \bar{\mathbf{x}}^a)(\mathbf{x}_i^a - \bar{\mathbf{x}}^a)^T = \sum_{i=1}^K w_i (\mathbf{x}_i^f - \bar{\mathbf{x}}^f)(\mathbf{x}_i^f - \bar{\mathbf{x}}^f)^T \quad , \quad (14)$$

24 Where \mathbf{P}^a is the error covariance matrix of the analysis ensemble, calculated by the perturbation of the analysis ensemble.

25 In NETF, \mathbf{A} performs as a transform matrix like the transform matrix (\mathbf{T}) in ETKF, which can be obtained from the weight
26 matrix (\mathbf{w}).

$$27 \quad \mathbf{P}^a = \mathbf{X}^{f'} \mathbf{A} \mathbf{X}^{f'}^T \quad , \quad (15)$$

$$28 \quad \mathbf{A}^{1/2} = (\mathbf{W} - \mathbf{w}\mathbf{w}^T)^{1/2} = \mathbf{V} \mathbf{D}^{1/2} \mathbf{V}^T \quad , \quad (16)$$

29 Where the matrix $\mathbf{W} \equiv \text{diag}(\mathbf{w})$ is defined as a diagonal matrix created from the weight matrix (\mathbf{w}). \mathbf{A} can be decomposed

30 ($\mathbf{A} = \mathbf{V}\mathbf{D}\mathbf{V}^T$) by a singular value decomposition as it is a real, symmetric, positive semidefinite matrix. \mathbf{V} is the orthogonal
31 matrix, and \mathbf{D} is a diagonal matrix.

32

33 Then, the perturbation of the analysis ensemble ($\mathbf{X}^{a'}$) and the analysis ensemble (\mathbf{X}^a) can be obtained by applying the square
34 root of \mathbf{A} as a transform matrix.

$$35 \mathbf{X}^{a'} = \sqrt{\mathbf{K}}\mathbf{X}^f \mathbf{A}^{1/2}, \quad (17)$$

$$36 \mathbf{X}^a = \bar{\mathbf{X}}^f + \mathbf{X}^f (\bar{\mathbf{W}} + \sqrt{\mathbf{K}}\mathbf{A}^{1/2}), \quad (18)$$

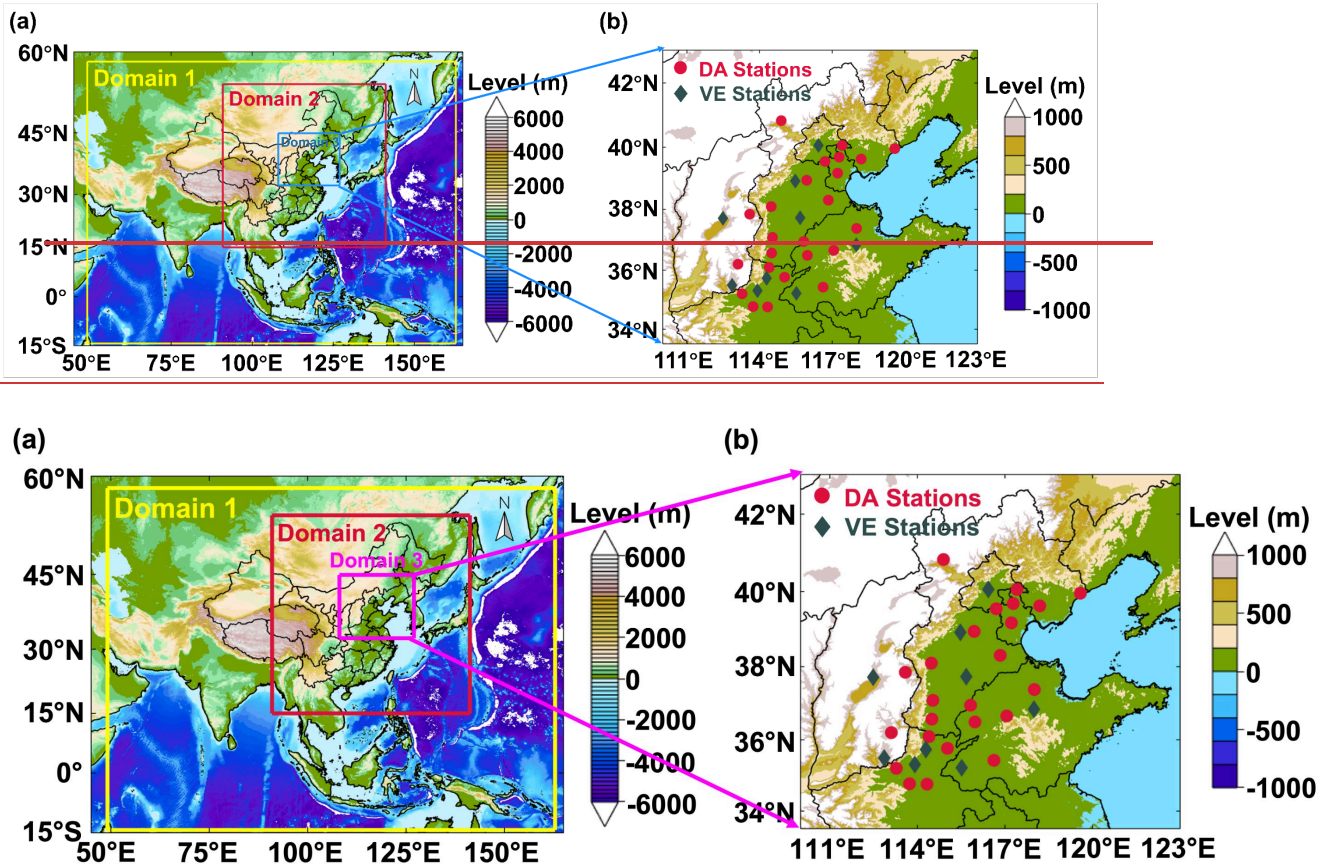
37 LKNETF combines the LETKF and LNETF through a hybrid weight γ to perform better in systems with different non-
38 linearity degrees and implement in situations with smaller ensemble sizes (Nerger, 2022). When γ approaches 1, the analysis
39 increment ($\Delta\mathbf{X}_{\text{LETKF}}$) computed by LETKF becomes more significant and appropriate for linear systems with Gaussian
40 distributions. Conversely, when γ approaches 0, the analysis increment ($\Delta\mathbf{X}_{\text{LNETF}}$) computed by LNETF becomes more
41 significant and appropriate for non-linear systems with non-Gaussian distributions. The one-step update scheme is used in this
42 study.

$$43 \mathbf{X}_{\text{HSync}}^a = \bar{\mathbf{X}}^f + (1 - \gamma)\Delta\mathbf{X}_{\text{LNETF}} + \gamma\Delta\mathbf{X}_{\text{LETKF}}, \quad (19)$$

44 2.4 Data

45 2.4.1 Observation

46 The one-month (February 2022) hourly mass concentration observations of five $\text{PM}_{2.5}$ chemical components (NH_4^+ , SO_4^{2-} ,
47 NO_3^- , OC, and EC) from 33 ground-based sites in Northern China and surrounding areas were collected for this work (Fig. 3).
48 Out of the 33 sites, 24 (DA sites) were utilized for DA and internal validation, and the remaining 9 (VE sites) were used for
49 independent verification to assess the influence of DA sites on neighboring areas. These sites were divided using the K-means
50 clustering algorithm (Lloyd, 1982; Arthur and Vassilvitskii, 2007). The supplement provides a detailed description (Text S1).
51 $\text{PM}_{2.5}$ hourly observations from the China National Environmental Monitoring Centre (CNEMC, <http://www.cnemc.cn/>) were
52 employed to assess the overall mass concentration of $\text{PM}_{2.5}$ chemical components in NAQPMS-PDAF v2.0. Due to incomplete
53 spatial overlap between the $\text{PM}_{2.5}$ sites and the chemical component sites, the $\text{PM}_{2.5}$ sites were selected based on the closest
54 ~~coordinate~~-Euclidean distance between $\text{PM}_{2.5}$ sites and chemical component sites.



55

56

57 Figure 3: The model domains in WRF simulation (a) and the location of observations (b). ~~The domain Domain 3~~ in (a) is the target
 58 area ~~in~~ of this study. Twenty-four red sites in (b) represent the sites for data assimilation, and nine green sites in (b) represent the
 59 sites for spatial independent validation. The topographic dataset is from the ETOPO1 1 arc-minute Global Relief Model, taken from
 60 the National Geophysical Data Center (Amante and Eakins, 2009).

61 **2.4.2 Global reanalysis dataset**

62 The global reanalysis datasets of PM_{2.5} chemical components in February 2022 were obtained from the Copernicus Atmosphere
 63 Monitoring Service ReAnalysis (CAMSR, 0.75°×0.75°) (Inness et al., 2019) and the Modern-Era Retrospective analysis for
 64 Research and Applications, Version 2 (MERRA-2, 0.5°×0.625°) (Randles et al., 2017) to compare with reanalysis dataset
 65 generated by NAQPMS-PDAF v2.0. For the ~~data consistency-of data-comparison~~, the global reanalysis surface grid data
 66 located in the observation sites of PM_{2.5} chemical component were extracted through the k-nearest neighbor search method
 67 (Friedman et al., 1977), which can efficiently match grid points and observation sites based on longitude and latitude data and
 68 Euclidean distances. Our 3-hourly NAQPMS-PDAF v2.0 output of NO₃⁻ and NH₄⁺ were extracted to compare with the
 69 CAMSR dataset, and hourly NAQPMS-PDAF v2.0 output of SO₄²⁻, OC, and EC were extracted to compare with MERRA-
 70 2 M2T1NXAER dataset.

71 **2.5 Experimental setting and evaluation method**

72 In our study, four tests were conducted to evaluate the performance of NAQPMS-PDAF v2.0 with hourly observations of five

73 PM_{2.5} chemical components, including (1) the dependence on ensemble size and assimilation frequency, (2) the interpretation
74 ability on mass concentration and spatiotemporal characteristics, (3) the superiority quality of output data compared to other
75 reanalysis dataset/datasets, and (4) the uncertainty in ensemble assimilation. In practice, the ratio of ensemble size to the number
76 of processes with 1:50 in high-performance computers was the bestoptimal parallel scheme to balance computing efficiency
77 and computing resources (Wang et al., 2022).

78
79 All the tests were run in NAQPMS-PDAF v2.0 after a spin-up experiment with 24 timesteps from 00:00 to 23:00 (LST) on
80 February 1st, 2022. (1) For the first test, we assimilated the hourly observations of five PM_{2.5} chemical components from all
81 sites with 48 timesteps from 00:00 (LST) on February 2nd to 23:00 (LST) on February 3rd, 2022. In the first situationscenario,
82 we controlled a fixed assimilation frequency of 1 hour and changed the ensemble size to 2, 5, 10, 15, 20, 30, 40, and 50. In the
83 second situationscenario, we controlled a fixed ensemble size of 20 and changed the assimilation frequency to 1 hour, 2 hours,
84 3 hours, 4 hours, 5 hours, 6 hours, 8 hours, and 12 hours. (2) For the second test, we set an ensemble size of 20 and an
85 assimilation frequency of 1 h and assimilated the hourly observations of five PM_{2.5} chemical components from DA sites with
86 648 timesteps from 00:00 (LST) on February 2nd to 23:00 (LST) on February 28th, 2022. We also conducted a free running
87 (FR) experiment without assimilation in the same period for comparison. (3) For the third test, we followed the settings in the
88 second test but assimilated the observation from all sites to generate a high-quality reanalysis dataset of five PM_{2.5} chemical
89 components. (4) The lastfinal test was likeanalogous to the first test but with a different situation to investigate distinct scenario
90 designed to examine the impactinfluence of ensemble perturbation on ensemble assimilation. From Table 2, we fixed species
91 uncertainty (M4 setting) with five distribution types in the first situationscenario and fixed distribution type (T2 setting) with
92 five SO₂ uncertainties in the second.

93 **Table 2: The experiment settings for emission perturbation**

Experiment	Distribution (Fixed species uncertainty)
T1	Gaussian
T2	Non-Gaussian (m3=1, m4=6)
T3	Non-Gaussian (m3=-1, m4=6)
T4	Non-Gaussian (m3=1, m4=12)
T5	Non-Gaussian (m3=-1, m4=12)
SO ₂ uncertainty (Fixed distribution)	
M1	12%
M2	50%
M3	100%
M4	200%
M5	300%

94
95 We used the Continuous Ranked Probability Score (CRPS) to evaluate ensemble size dependency, which measures the

96 consistency between ensemble forecast distribution and corresponding observations (Jolliffe and Stephenson, 2012). The
97 calculation rules are referred to in Hersbach's study (Hersbach, 2000). Besides, four common statistical indicators, the Pearson
98 correlation coefficient (CORR), root mean square error (RMSE), mean absolute error (MAE), and coefficient of determination
99 (R^2), were used to assess the DA system performance in interpreting PM_{2.5} chemical components (SO₄²⁻, NO₃⁻, NH₄⁺, OC, and
00 EC). The CORR measures the correlation between the system outputs and corresponding observations, the RMSE and MAE
01 ~~indicates~~indicate the overall system accuracy, and the R^2 reflects the proportion of variability in the observations explained by
02 the assimilation system.

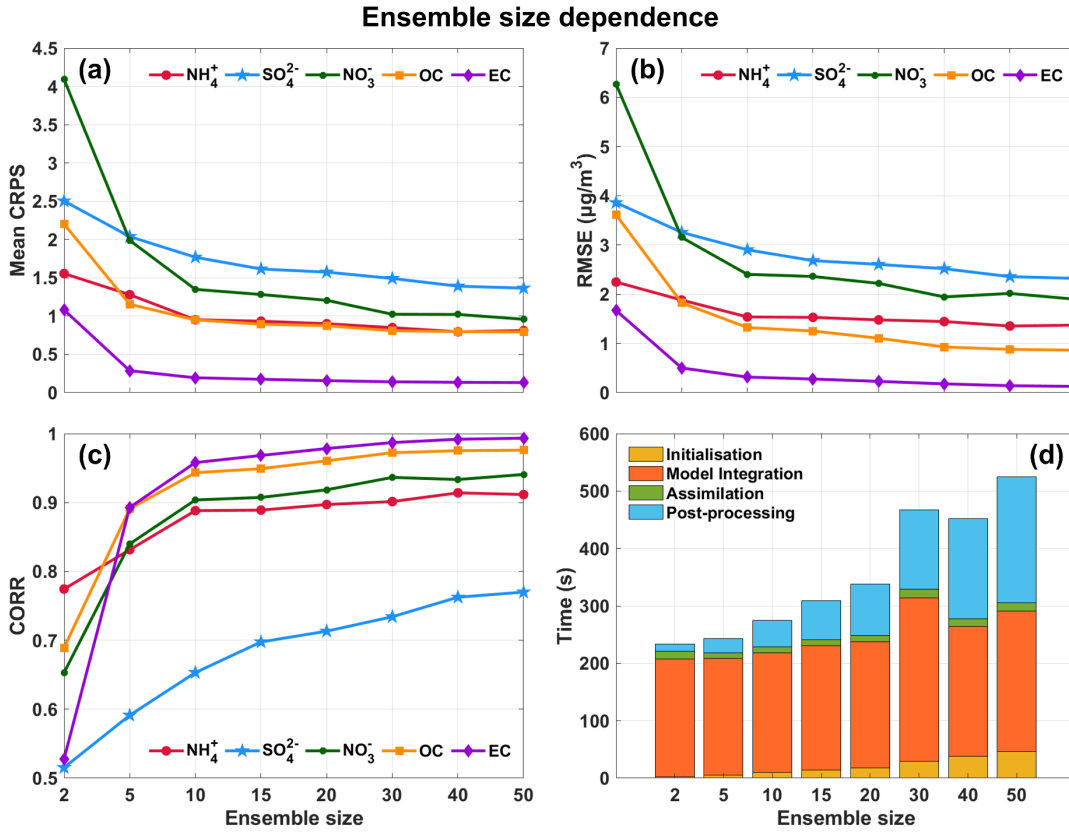
03 3 Results and discussion

04 3.1 The Dependence on Ensemble Size and Assimilation Frequency for Five Components

05 Ensemble size is a crucial parameter in ensemble assimilation, determining the model state's uncertainty range. A larger
06 ensemble size more accurately represents the error distribution of state variables but requires considerable computing resources
07 and time, especially for high-dimension systems. A smaller ensemble size can easily lead to underestimating the error
08 covariance matrix, especially for the fine-resolution model (Kong et al., 2021). Thus, identifying an appropriate ensemble size
09 to balance computational efficiency and accuracy is the primary step in ensemble DA. A prior study (NAQPMS-PDAF v1.0)
10 only evaluated the correlation between ensemble size and parallel efficiency and concluded that the ratio of ensemble size to
11 high-performance computing processors was 1:50 (Wang et al., 2022), while the impact of ensemble size on the accuracy and
12 computational efficiency was neglected. ~~In this~~This study, ~~we~~ assessed the NAQPMS-PDAF v2.0 dependency on ensemble
13 size through three statistical indicators (CRPS, RMSE, and CORR). Figure 4 shows the mean CRPS, RMSE, and CORR values
14 and the statistical averages of the elapsed time over 48 timesteps with the ensemble sizes of 2, 5, 10, 15, 20, 30, 40, and 50.

15
16 From Fig. 4a, when the ensemble size is at its minimum level of 2, the mean CRPS values of the five PM_{2.5} chemical
17 components are more significant, with NO₃⁻ exhibiting the most considerable difference between the simulation distribution
18 and observations (more than 4). With each increase in ensemble size, the mean CRPS values of the five chemical components
19 progressively reduce and eventually reach convergence when the ensemble size is 10, implying that a hybrid nonlinear filter
20 can maintain high accuracy and reliability in ensemble assimilation with an ensemble size that is smaller than the traditional
21 minimum of 20 ensemble members, as observed in prior ensemble assimilation studies (Constantinescu et al., 2007; Miyazaki
22 et al., 2012; Schwartz et al., 2014; Rubin et al., 2017; Kong et al., 2021; Tsikerdekis et al., 2021; Wang et al., 2022), including
23 NAQPMS-PDAF v1.0. The mean CRPS value of EC is the lowest among the five chemical components, indicating the highest
24 accuracy and reliability of EC ensemble DA. The performance of other components is similar. Like CRPS values, the values

25 of RMSE and CORR decrease and increase, respectively, as the ensemble size increases, and convergence begins to occur
 26 when the ensemble size is 10 (Fig. 4b and c). Compared with other chemical components, the CORR value of SO_4^{2-} is
 27 significantly lower, less than 0.8, possibly due to its estimated background field error covariance driven by the inadequate
 28 ensemble perturbations. Therefore, in the Discussion section, we ~~deeply~~ discuss the uncertainties of ensemble perturbations.



29
 30 **Figure 4: Assessment of ensemble size dependency based on mean continuous ranked probability score (CRPS) (a), root mean square**
 31 **error (RMSE) (b), correlation coefficient (CORR) (c), and time (d).**

32 Figure 4d shows the time required for the four processes of ensemble assimilation under different ensemble sizes, including
 33 initialization, model integration, assimilation, and post-processing. The model integration process in NAQPMS-PDAF v2.0
 34 takes the longest, followed by post-processing, initialization, and assimilation. The required time for initialization and post-
 35 processing increases with increasing ensemble size, while for model integration and assimilation, except for ensemble size 30,
 36 the required time is the same under different ensemble sizes. Generally, the time needed for ensemble sizes of 30-50 is
 37 considerably higher than that for smaller ones. Although convergence occurs with an ensemble size of 10, our work illustrates
 38 a similar time required between ensemble sizes 10 and 20. Consequently, we selected an ensemble size of 20 to ensure optimal
 39 performance of NAQPMS-PDAF v2.0, considering both assimilation efficiency and accuracy.

40
 41 The assimilation frequency is the interval at which observational data is introduced into the DA system, directly affecting the
 42 practical assimilation data volume and computation cost. High-frequency DA with high-quality observations is crucial for

improving numerical simulations and forecasts (Liu et al., 2021). Figure 5 demonstrates that the MAE values of the five chemical components analysis fields range from 0.02 to 0.12 $\mu\text{g}/\text{m}^3$, RMSE values range from 0.23 to 2.61 $\mu\text{g}/\text{m}^3$, and CORR values range from 0.71 to 0.98 at a 1-hour assimilation time interval, which is significantly better than the statistical indicators at lower assimilation frequencies. Even at a 2-hour assimilation frequency, the assimilation effect drops sharply compared to the 1-hour interval, especially for NO_3^- , OC, and EC. The values of MAE and RMSE increase by 2.6-5.82 $\mu\text{g}/\text{m}^3$ and 4.72-9.57 $\mu\text{g}/\text{m}^3$, respectively, and the CORR values decrease by 0.27-0.81. Gradual increasing trends in MAE and RMSE values and a slight decreasing trend in CORR values are observed as assimilation frequency decreases from the 2-hour interval. Therefore, the fast-updating assimilation with a 1-hour interval significantly improves the NAQPMS simulation. For the forecasting field (Fig. S2), the low sensitivity of state variables to assimilation frequency suggests that NAQPMS-PDAF v2.0 can appropriately reduce assimilation frequency during the actual forecasting phase, lowering the demand for high temporal resolution observations and computational resources.

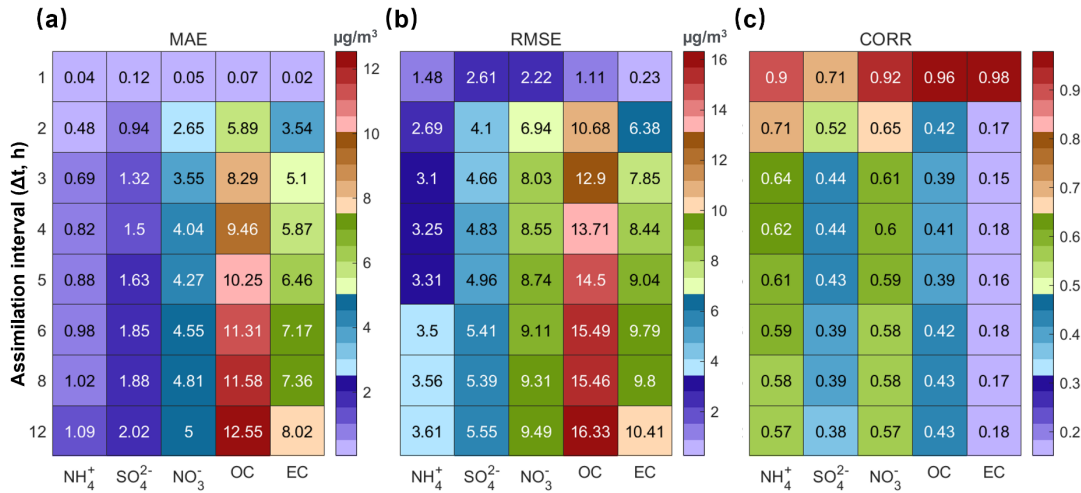


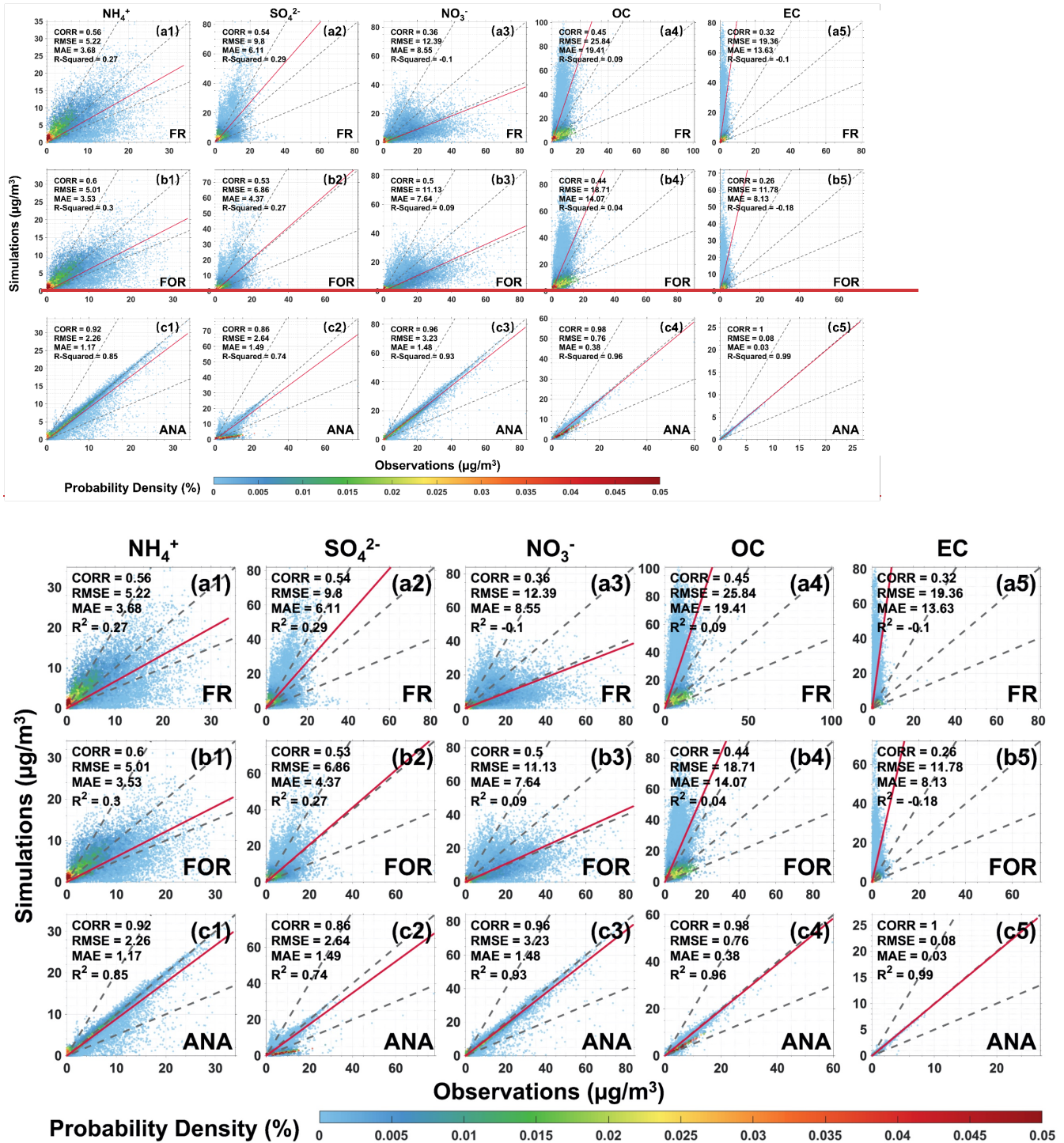
Figure 5: Assessment of assimilation interval dependency based on mean absolute error (MAE) (a), root mean square error (RMSE) (b), and correlation coefficient (CORR) (c) at the analysis step.

3.2 Evaluation of NAQPMS-PDAF v2.0 performance

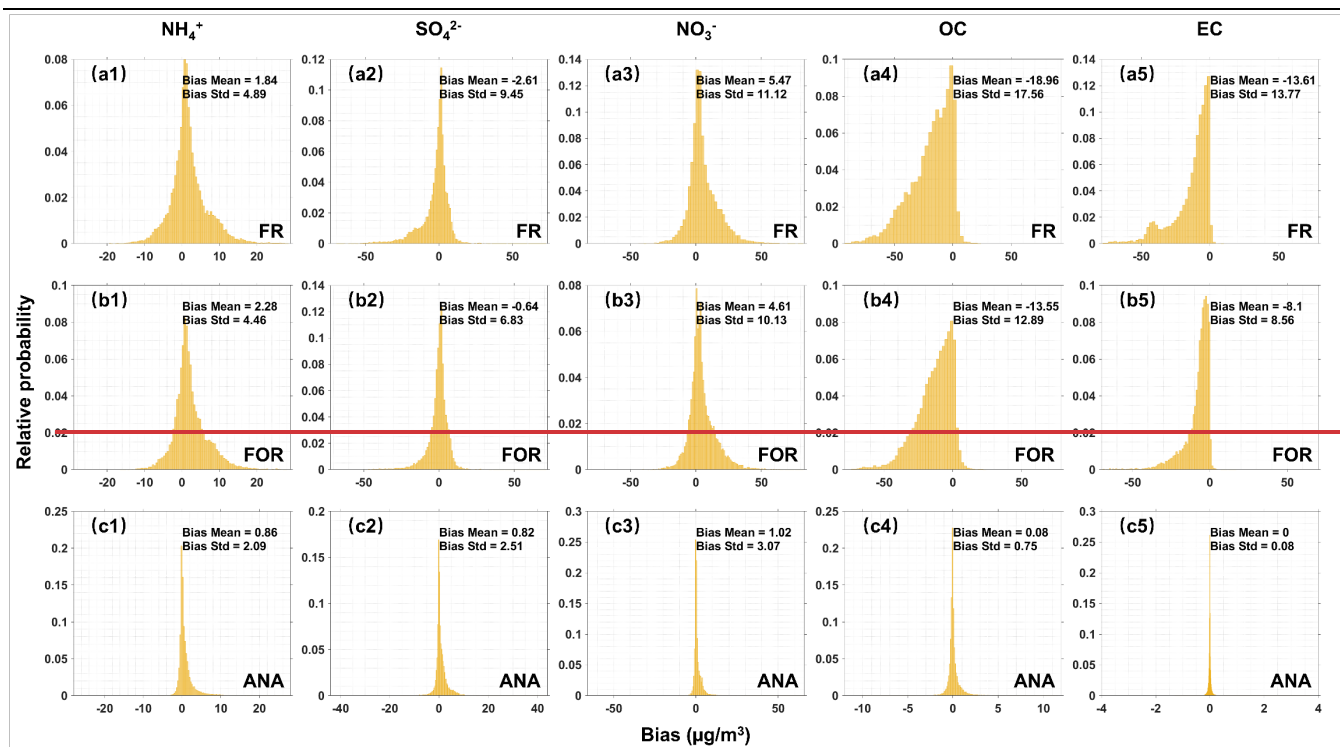
3.2.1 Overall validation of DA results

We conducted a control experiment (free-running field, FR) without any DA and a DA experiment. This section verified the forecast ~~field~~ (FOR) and analysis field (ANA) at 24 DA sites and 9 VE sites, respectively. Figure 6 shows the scatter distribution of observations and simulations at DA sites. For FR (Fig. 6a1-a5), five chemical components have CORR values ranging from 0.32 to 0.56, and R^2 values do not exceed 0.3, indicating poor consistency between observations and simulations. In detail, the simulated mass concentrations of SO_4^{2-} , OC, and EC are significantly overestimated, while the simulated concentrations of NH_4^+ and NO_3^- are underestimated. OC has the most significant error, with an RMSE value of 25.84 $\mu\text{g}/\text{m}^3$ and an MAE value of 19.41 $\mu\text{g}/\text{m}^3$. Besides, the error distributions of SO_4^{2-} , NO_3^- and NH_4^+ are close to a symmetric distribution

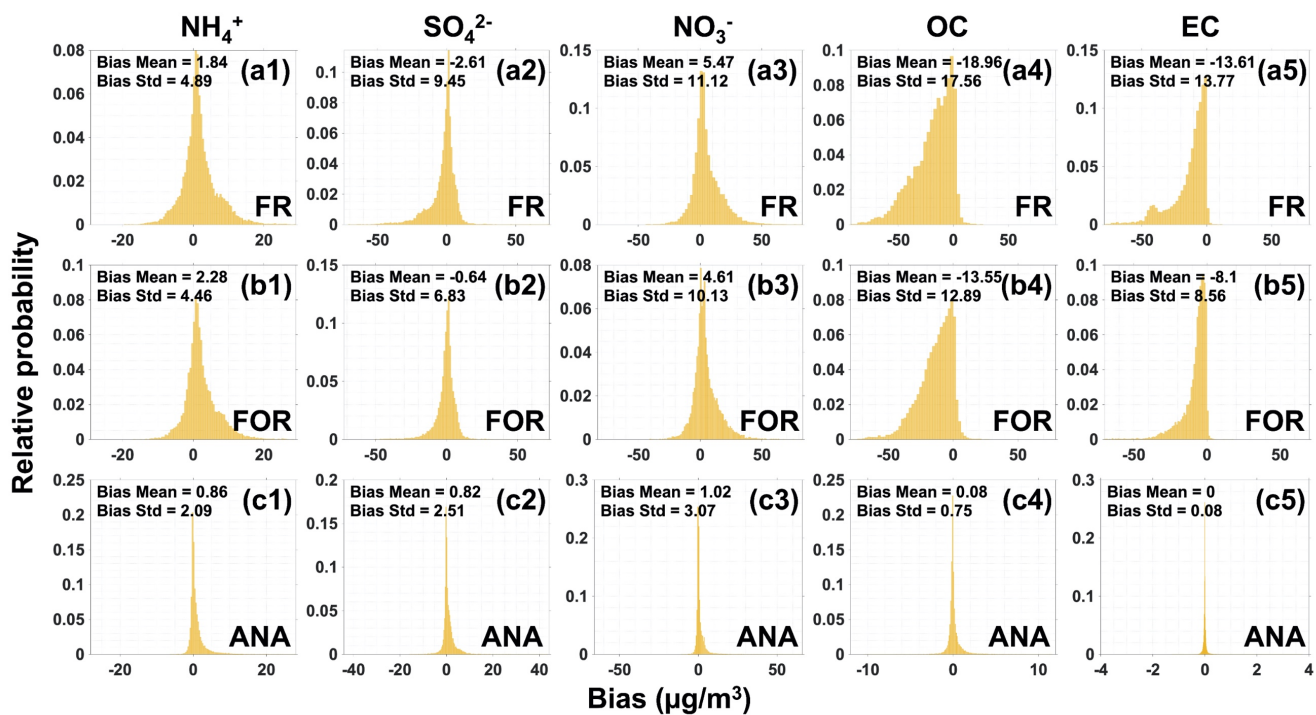
66 with a mean value of 0, while the error distributions of OC and EC are skewed to the left from the mean value of 0 (Fig. 7a1-
 67 a5), showing the relatively better simulations in SO_4^{2-} , NO_3^- and NH_4^+ than in OC and EC. Overall, NAQPMS cannot interpret
 68 the mass concentrations of the five chemical components with significant errors, mainly due to the uncertainties in chemical
 69 mechanisms (Miao et al., 2020).



71
 72 Figure 6: Scatterplots of the DA-site simulations versus the DA-site observations with probability density for the free-running field
 73 (FR, a1-a5), forecast field (FOR, b1-b5), and analysis field (ANA, c1-c5). The dotted gray lines represent the 2:1, 1:1, and 1:2 lines,
 74 and the solid red line represents the fitting regression line.



75



76

77

Figure 7: Probability distributions of bias between DA-site observations and DA-site simulations for the free-running field (FR, a1-a5), forecast field (FOR, b1-b5), and analysis field (ANA, c1-c5).

78

79

After DA, FOR shows a slight improvement with a slight increase in CORR and R² and a decrease in RMSE and MAE,

80

especially for NH₄⁺ and NO₃⁻ (Fig. 6b1-b5). Although SO₄²⁻, OC, and EC are significantly overestimated with a slight decrease

81

in CORR and R², the RMSE and MAE values decrease. Besides, the error distributions of the five chemical components are

82

concentrated at 0, and the overestimation of OC and EC has been improved compared to FR (Fig. 7b1-b5). These results

83

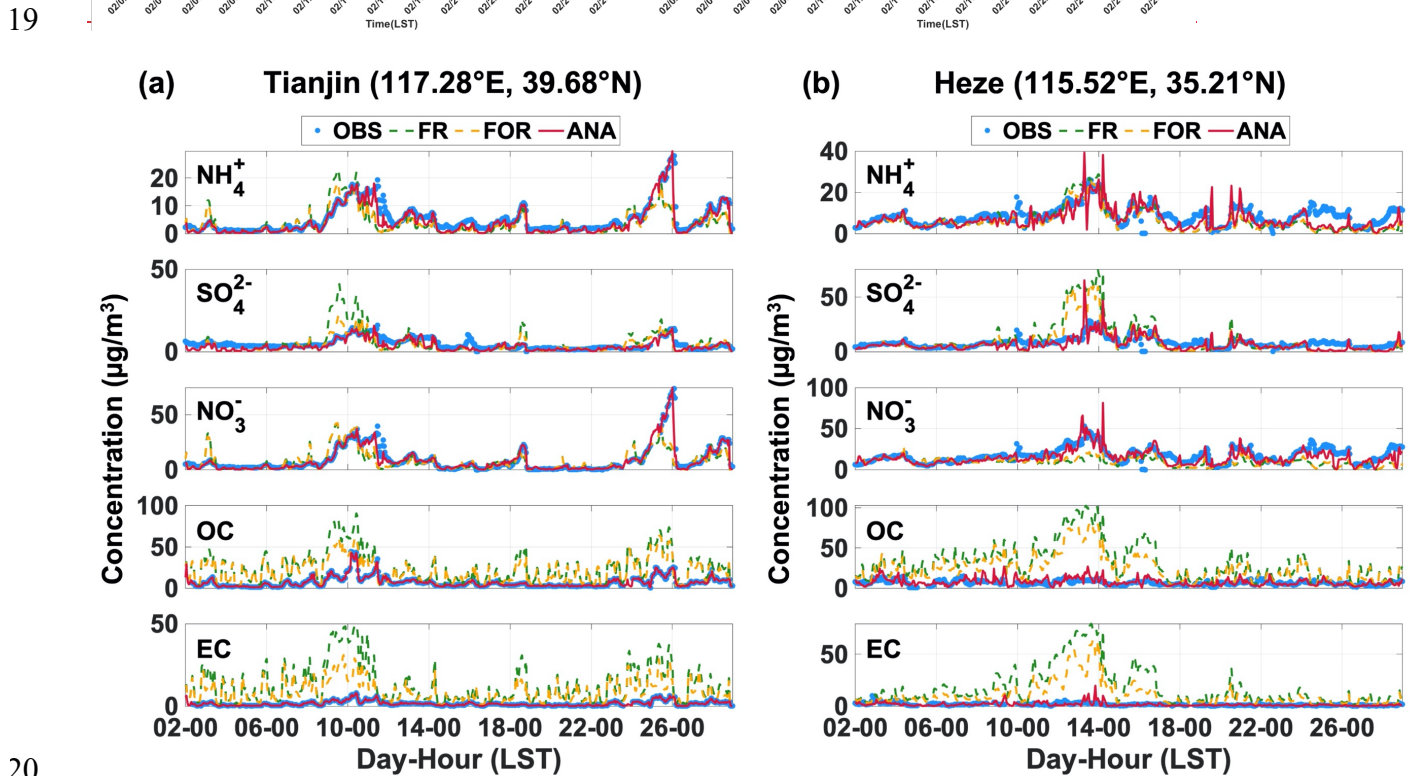
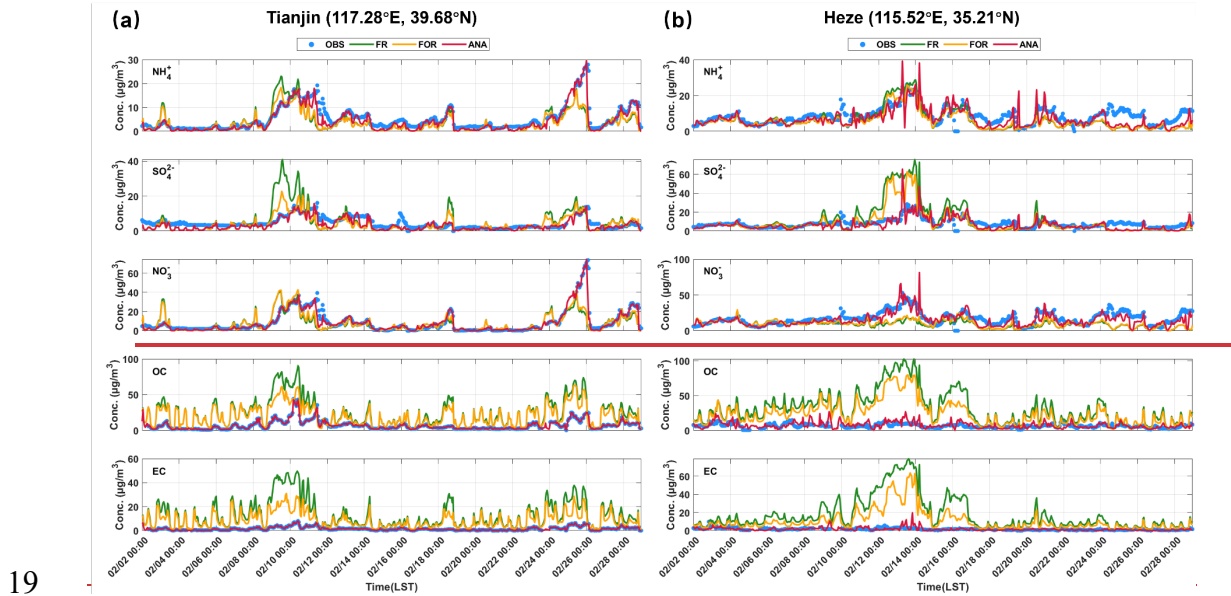
indicate that DA reduces the overall FOR errors in NAQPMs due to improved forecasting ability by obtaining optimal initial

84 fields. However, further improvements are necessary to address the NAQPMS uncertainties in emission sources,
85 meteorological input, and imperfect physiochemical mechanisms. For ANA (Fig. 6c1-c5), DA significantly improves the
86 simulations of the five chemical components, making the ANA consistent with the observations. The CORR values are not
87 less than 0.86, the RMSE and MAE values do not exceed $3.23 \mu\text{g}/\text{m}^3$ and $1.49 \mu\text{g}/\text{m}^3$, respectively, and the R^2 values are not
88 less than 0.74. Specifically, the CORR values for NO_3^- , OC, and EC are not less than 0.96, and the R^2 values are not less than
89 0.93. The error distributions of the five chemical components concentrate to 0 with the mean bias ranging from $0 \pm 0.08 \mu\text{g}/\text{m}^3$
90 to $1.02 \pm 3.07 \mu\text{g}/\text{m}^3$ (Fig. 7c1-c5). The results of VE sites show similar characteristics to the DA sites (Fig. S3 and S4).
91 Compared to FR, the overall errors of the FOR and ANA for the five chemical components decrease with a significant
92 improvement in ANA, showing that the CORR values of NH_4^+ and NO_3^- increase by 0.15 and 0.45, respectively, the R^2 values
93 of NH_4^+ and NO_3^- increase by 0.22 and 0.81, respectively, the RMSE values of OC and EC decrease by $21.77 \mu\text{g}/\text{m}^3$ and 17.79
94 $\mu\text{g}/\text{m}^3$, respectively. Overall, the FOR and ANA errors decreased significantly. The ANA of the five chemical components at
95 DA sites is almost entirely consistent with the observations, indicating excellent DA performance.

96 3.2.2 Assessment of temporal variation in chemical components

97 The ensemble DA employs a cyclic updating process wherein the forecast and analysis steps are continuously completed at
98 each iteration (Evensen, 2003; Houtekamer and Zhang, 2016). In the forecast step, the ANA at the current time step serves as
99 the optimal initial field to advance the model integration and obtain the FOR at the next step. In the analysis step, the FOR at
00 the next time step provides background field information for the subsequent DA analysis to generate the ANA at the next time
01 step. The FOR and ANA interact with each other in the temporal dimension. Therefore, in this section, we assess the ability of
02 NAQPMS-PDAF v2.0 to interpret the temporal variations of the five chemical components. Figure 8 illustrates the time series
03 of the five chemical components at two representative sites, including a DA site in Tianjin City and a VE site in Heze City. For
04 the DA site (Fig. 8a), the temporal variations of NH_4^+ and NO_3^- in FR and FOR exhibit better agreement with the observed
05 temporal variations (OBS) than those of SO_4^{2-} , OC, and EC. However, NH_4^+ and NO_3^- mass concentrations are significantly
06 lower than the high-value mass concentrations observed on February 25th. The mass concentration of SO_4^{2-} in FR is greatly
07 overestimated during the periods of Feb. 8th-11th, Feb. 18th-19th, and Feb. 24th-25th. The mass concentrations of OC and EC in
08 FR are overestimated throughout February with substantial temporal fluctuations. Although the time series of SO_4^{2-} , OC, and
09 EC in FOR show some improvement, noticeable differences from the OBS are still apparent. After DA, the ANA time series
10 for the five chemical components align well with the OBS, indicating good consistency and accurate representation of temporal
11 characteristics, such as the NH_4NO_3 pollution captured on February 25th. Notably, the mass concentrations of SO_4^{2-} , NO_3^- , and
12 NH_4^+ peaked on Feb. 8th-11th and February 25th, indicating intensified atmospheric secondary chemical reactions primarily due
13 to neutralization reactions of acidic pollutants capturing NH_3 . The temporal variations of NH_4^+ and NO_3^- are more similar

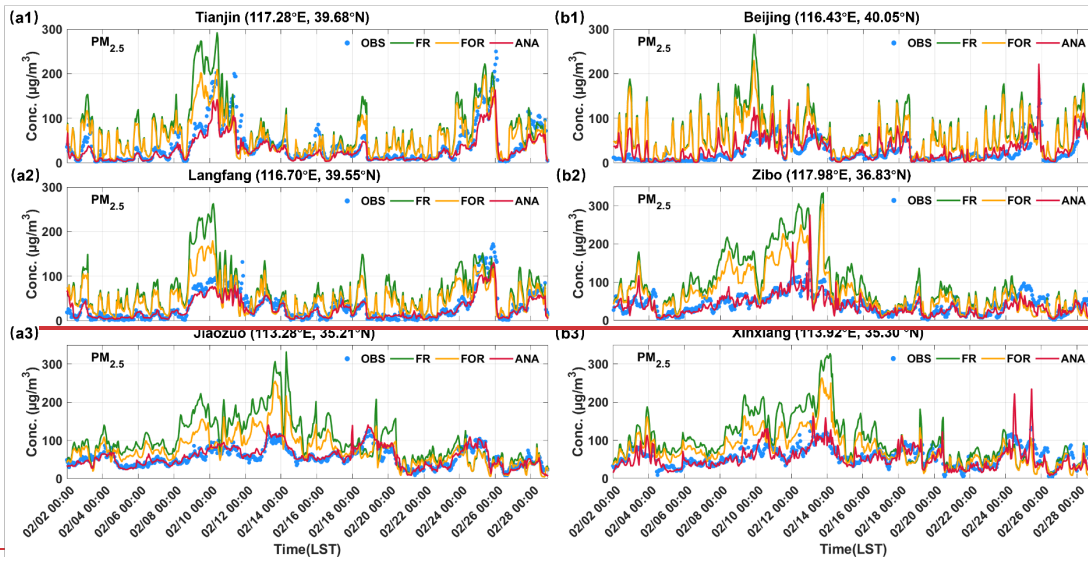
14 because atmospheric NO_3^- primarily mainly exists as NH_4NO_3 rather than other metal nitrates, and NH_4NO_3 can form before
 15 the complete neutralization of H_2SO_4 (Ge et al., 2017). The improvements at the VE site (Fig. 8b) are like those at the DA site,
 16 with the ANA time series of the five chemical components showing closer agreement with the OBS, which suggests that the
 17 localization analysis in DA effectively facilitates the propagation of observations within a specific spatial range and mitigates
 18 the assimilation anomalies caused by spurious correlations from the distant sites (Hunt et al., 2007).

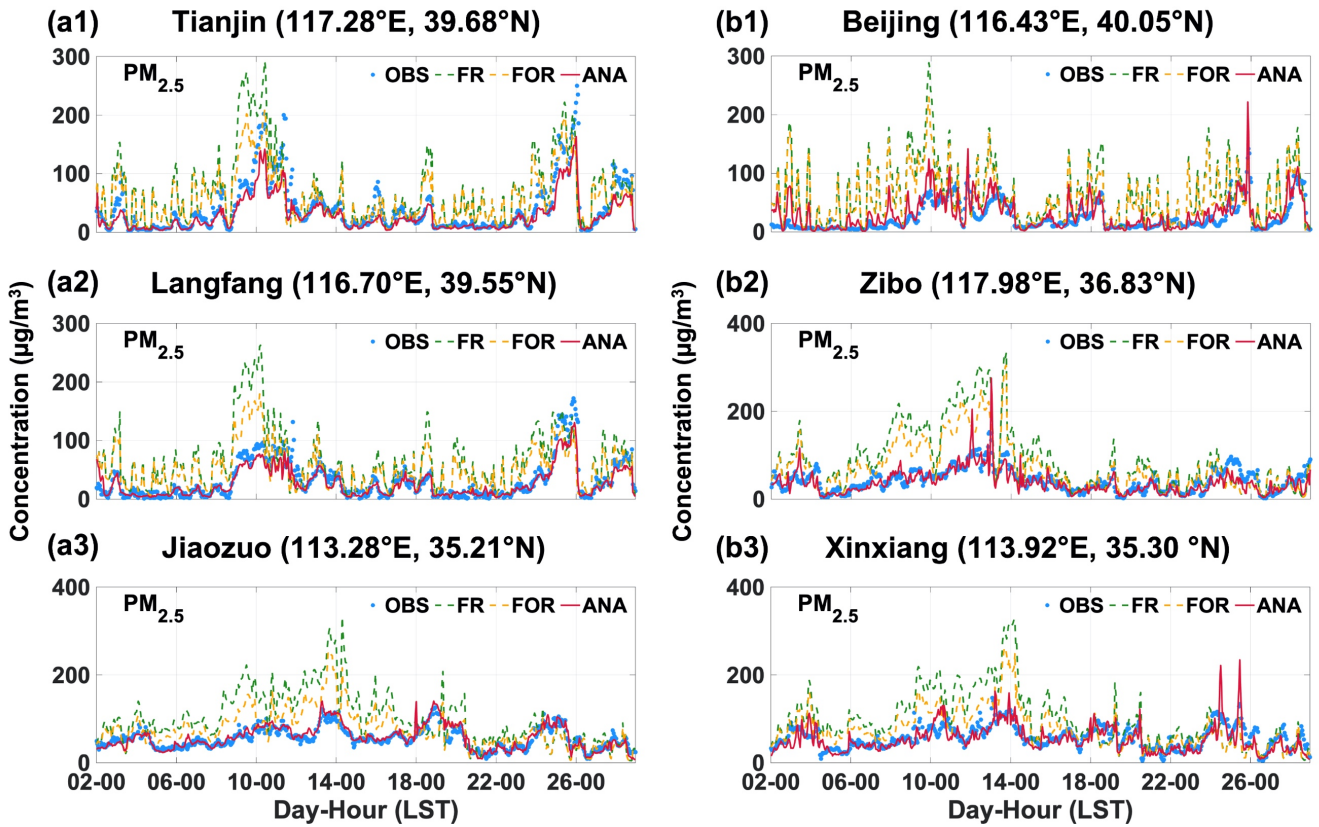


20
 21 **Figure 8: Hourly variation of five $\text{PM}_{2.5}$ chemical components in a representative DA site (a) and a representative VE site (b).**

22 NH_4^+ , SO_4^{2-} , NO_3^- , OC, and EC are critical chemical components of $\text{PM}_{2.5}$, and the sum of their mass concentrations can be
 23 approximated as the $\text{PM}_{2.5}$ mass concentration. We further assessed the simulation enhancement of $\text{PM}_{2.5}$ time series based on

24 ground-level PM_{2.5} observations. Six representative sites were selected, including 3 DA sites (Fig. 9a1-a3) and 3 VE sites (Fig.
25 9b1-b3). The FR and FOR in DA and VE sites show significant overestimation and poor consistency with the OBS, mainly
26 due to the overestimation of OC and EC mass concentrations. Conversely, the PM_{2.5} time series in ANA closely matches that
27 of the OBS, accurately capturing the actual variation of PM_{2.5}. In some specific instances, such as on February 26th at 00:00 in
28 Tianjin City and Langfang City, the peak value of ANA was lower than that of OBS, which could be attributed to the negligence
29 of other PM_{2.5} components (such as mineral dust and sea salt) and the inconsistency in location between ground-level PM_{2.5}
30 observational sites and chemical components observational sites. Overall, the DA of chemical component observations
31 significantly enhanced the simulation of PM_{2.5} time series in NAQPMS. Compared to the CORR values of FR and FOR, the
32 CORR values of ANA at the six representative sites increased by 13.64%-89.58% and 17.19%-75.00%, respectively, while the
33 RMSE values decreased by 56.03%-83.13% and 40.74%-72.20% (Table S3).





35

36

Figure 9: Hourly variation of PM_{2.5} in three representative DA sites (a1-a3) and three representative VE sites (b1-b3).

37

3.2.3 Assessment of spatial distribution in chemical components

38

DA can improve the interpretation of model states in the analysis domain by using a limited number of observations. The

39

ability to represent spatial distribution accurately is a crucial performance for aerosol DA. Figure 10 displays the spatial

40

distribution of the monthly average mass concentrations for the five chemical components, including OBS, FR, FOR, ANA,

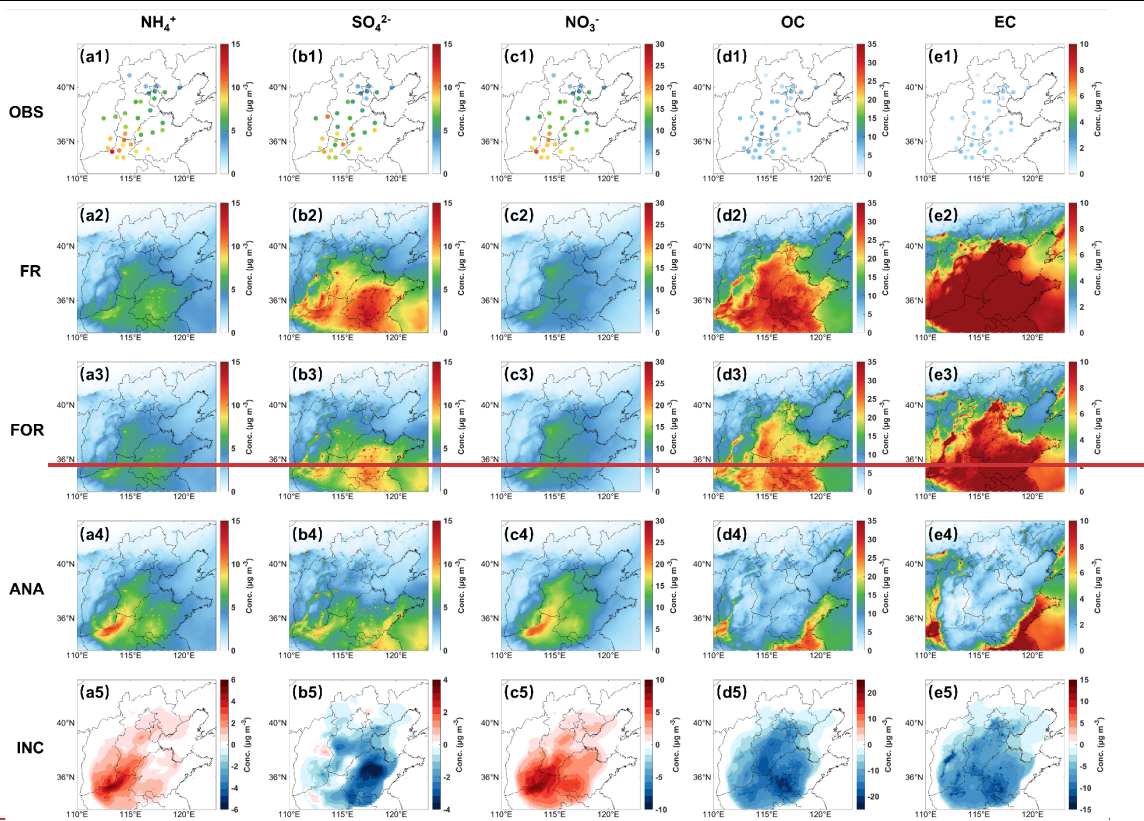
41

and analysis increment (INC). The spatial distributions of bias and statistical indicators for FR, FOR, and ANA are shown in

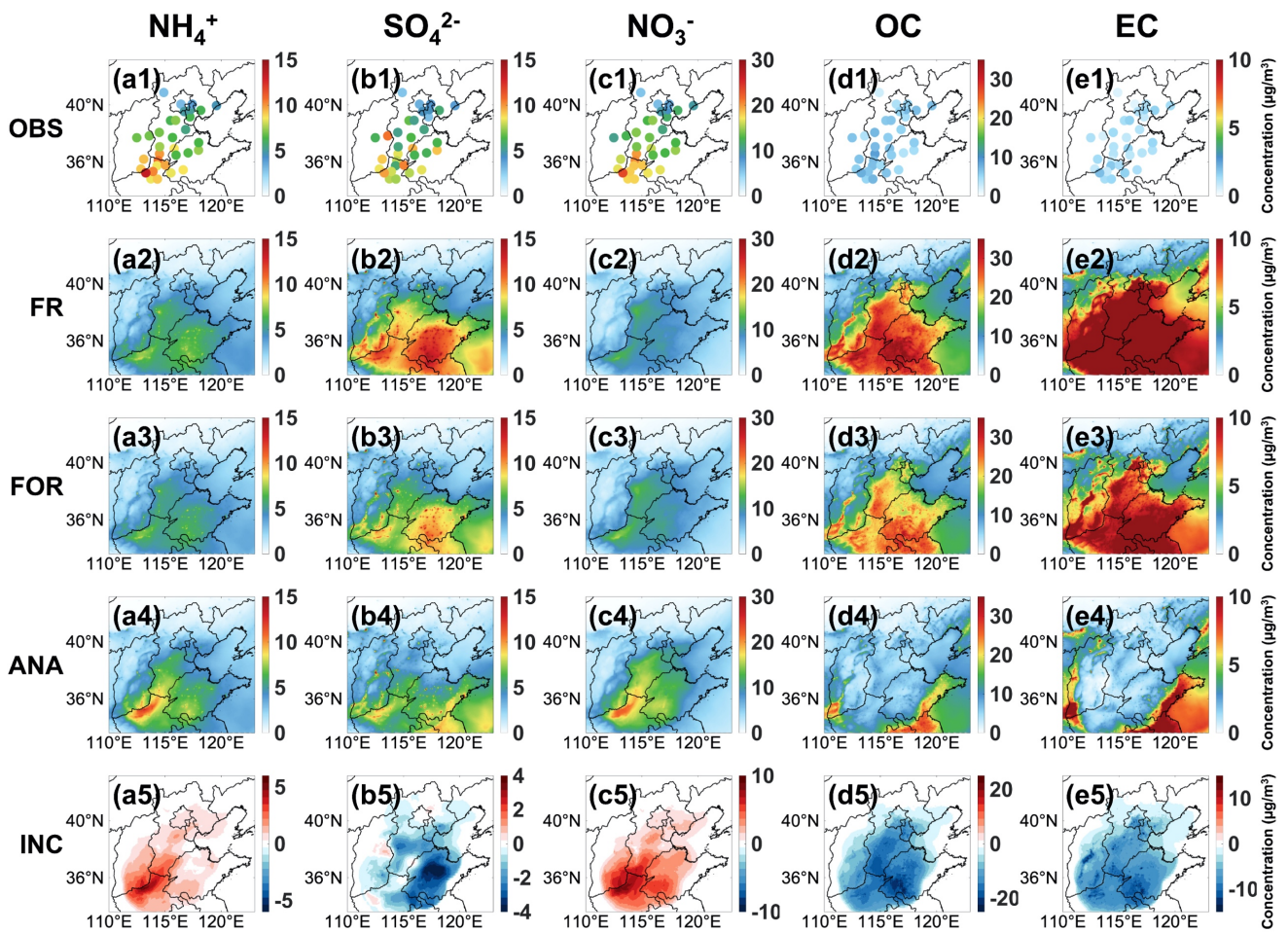
42

Fig. 11 and Fig. 12, respectively.

43



44

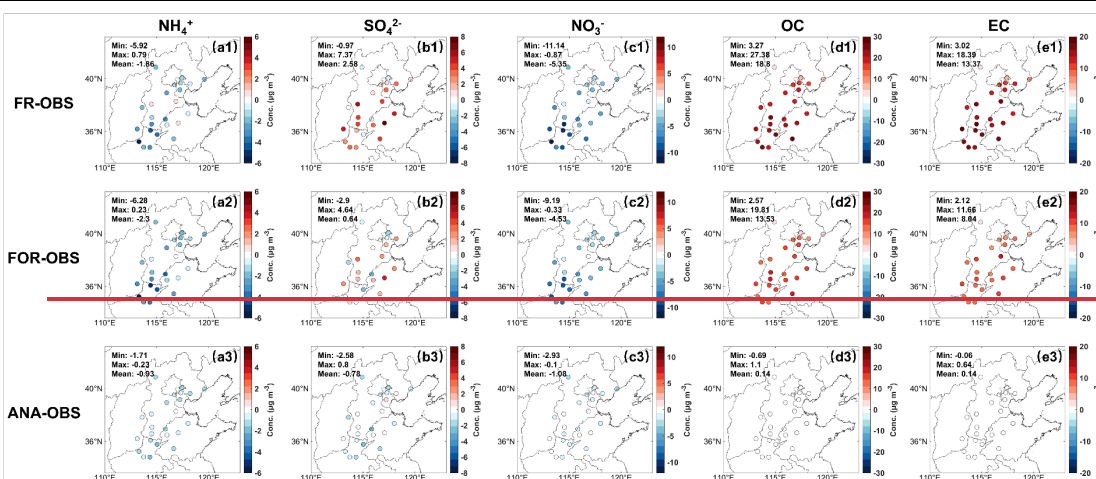


45

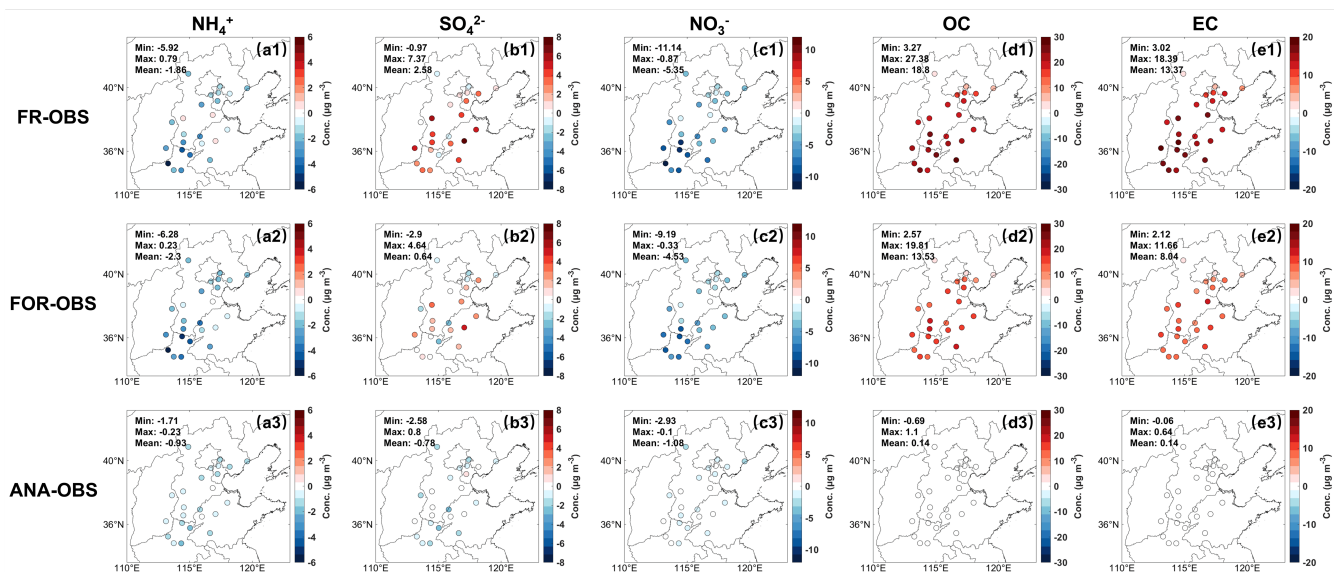
Figure 10: Spatial concentration distribution of site observation (OBS, a1-e1), free-run field (FR, a2-e2), forecast field (FOR, a3-e3), analysis field (ANA, a4-e4), and increment (INC) between ANA and FR (a5-e5) for five PM_{2.5} chemical components.

46

47



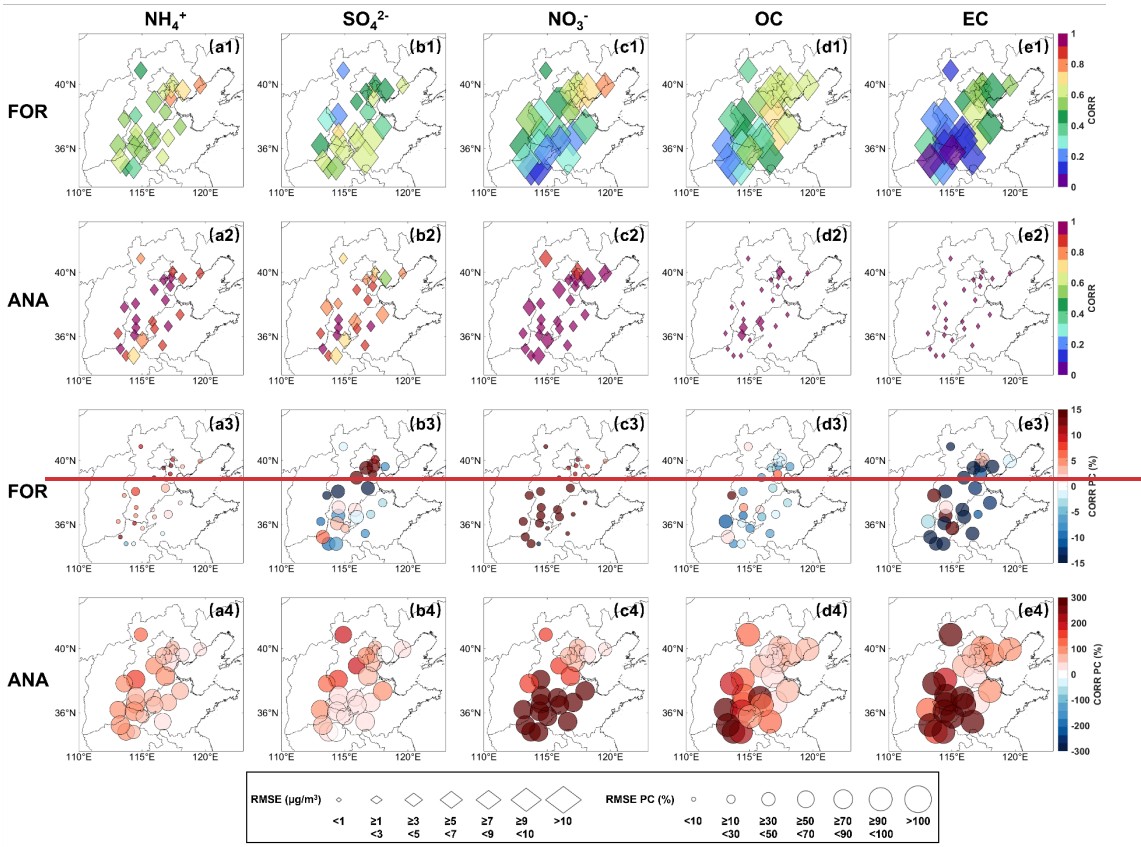
48

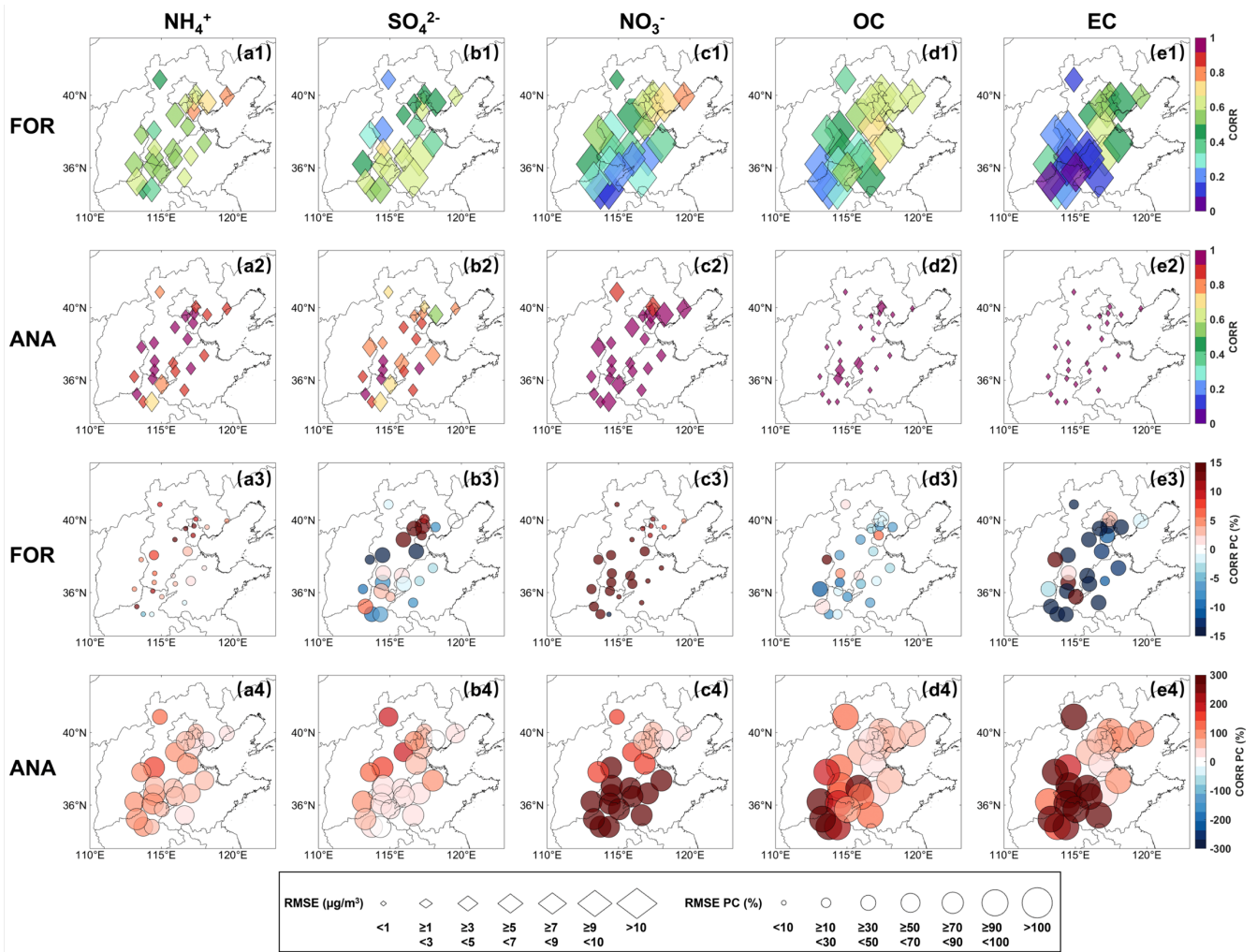


49

Figure 11: Spatial distribution of DA-site bias for five PM_{2.5} chemical components from observation (OBS) for the free-running field (FR, a1-e1), forecast field (FOR, a2-e2) and analysis field (ANA, a3-e3).

50





52

53 **Figure 12: Spatial distribution of DA-site statistical indicators for five PM_{2.5} chemical components. (a1-e1) represents the**
 54 **values of RMSE and CORR for the forecast field (FOR), (a2-e2) same as (a1-e1) but for analysis field (ANA), (a3-e3) represents the**
 55 **improvement of RMSE and CORR for the forecast field (FOR), (a4-e4) same as (a3-e3) but for analysis field (ANA). The size**
 56 **represents the value of RMSE in (a1-e2) and the improvement percentage compared to non-assimilation in (a3-e4), respectively.**

57 The spatial characteristics of NH₄⁺ and NO₃⁻ are similar. Compared to the OBS (Fig. 10a1 and c1), the FR (Fig. 10a2 and c2)
 58 and FOR (Fig. 10a3 and c3) have failed to capture the high-value mass concentrations in the border area between Hebei
 59 province, Shanxi province, Henan province, and Shandong province, especially in the northern region of Henan province. The
 60 primary reason is the uncertainties in emission inventories in winter heating periods, which results in insufficient emission
 61 statistics of gaseous precursors NO_x and NH₃ (Aleksankina et al., 2018). After DA, this situation is significantly improved
 62 with the ANA (Fig. 10a4 and c4). The INCs in the Beijing-Tianjin-Hebei region, Shanxi province, Henan province, and
 63 Shandong province are positive (Fig. 10a5 and c5), indicating varying degrees of improvement in correcting the
 64 underestimation of mass concentrations. Specifically, for NH₄⁺ and NO₃⁻ at DA sites, the biases between the OBS and ANA
 65 are significantly reduced compared to the biases between the OBS and FR (Fig. 11), with the mean absolute bias decreasing
 66 by 0.93 µg/m³ and 4.27 µg/m³, respectively. Moreover, the overall biases at VE sites also decrease (Fig. S5). As for the spatial

67 statistical indicators of NH_4^+ (Fig. 12a1 and a2), the CORR values in FOR and ANA range from 0.39 to 0.79 and 0.70 to 0.97,
68 respectively, and the RMSE values range from $3.16 \mu\text{g}/\text{m}^3$ to $7.65 \mu\text{g}/\text{m}^3$ and $1.20 \mu\text{g}/\text{m}^3$ to $3.49 \mu\text{g}/\text{m}^3$, respectively. As for
69 the spatial statistical indicators of NO_3^- (Fig. 12c1 and c2), the CORR values in FOR and ANA range from 0.09 to 0.76 and
70 0.89 to 0.99, respectively, and the RMSE values range from $4.88 \mu\text{g}/\text{m}^3$ to $15.69 \mu\text{g}/\text{m}^3$ and $1.34 \mu\text{g}/\text{m}^3$ to $5.39 \mu\text{g}/\text{m}^3$,
71 respectively. For the FOR, the improvement in accuracy for NO_3^- is more significant than that for NH_4^+ , with the CORR values
72 of most DA sites increasing by more than 10% and the RMSE of most DA sites decreasing by not less than 10% (Fig. 12a3
73 and c3). For the ANA, NH_4^+ and NO_3^- exhibit significant improvements in CORR and RMSE, as most DA sites show over
74 150% in CORR and over 50% in RMSE (Fig. 12a4 and c4). ~~The improvements~~Improvements can also be found ~~for~~in NH_4^+
75 and NO_3^- at VE sites (Fig. S6). The spatial consistency of NH_4^+ and NO_3^- indicates that NH_4NO_3 is the primary aerosol chemical
76 component, highlighting the necessity of coordinated control of precursor NO_x and NH_3 .

77
78 Unlike NH_4^+ and NO_3^- , compared to the OBS (Fig. 10b1), the mass concentrations of SO_4^{2-} in the FR and FOR (Fig. 10b2 and
79 b3) are significantly overestimated, especially in Shandong province. In contrast, the ANA has dramatically improved (Fig.
80 10b4), with most areas showing negative INCs (Fig. 10b5). The mean absolute biases in DA and VE sites have decreased by
81 $1.80 \mu\text{g}/\text{m}^3$ and $2.68 \mu\text{g}/\text{m}^3$, respectively (Fig. 11 and Fig. S5). Specifically, after DA, the CORR values of the FOR and ANA
82 range from 0.22 to 0.71 and 0.58-0.97, and the RMSE values range from $3.42 \mu\text{g}/\text{m}^3$ to $11.07 \mu\text{g}/\text{m}^3$ and $1.20 \mu\text{g}/\text{m}^3$ to 4.30
83 $\mu\text{g}/\text{m}^3$, respectively (Fig. 12b1 and b2). The CORR and RMSE values in FOR have significantly improved (Fig. 12b3) at DA
84 sites around Beijing. While the CORR values in ANA have increased by more than 13%, with most DA sites showing an
85 increase of over 50%, and RMSE values have decreased by no less than 30%, with most DA sites showing a decrease of over
86 70% (Fig. 12b4). Besides, half of the VE sites show significant improvement in the CORR and RMSE in the FOR and ANA,
87 mainly due to their proximity to more DA sites (Fig. S6). The OBS and ANA indicate a considerable control in SO_4^{2-} pollution
88 during the winter heating period due to the emission reduction of gaseous precursors (Zhai et al., 2019; Yan et al., 2021).

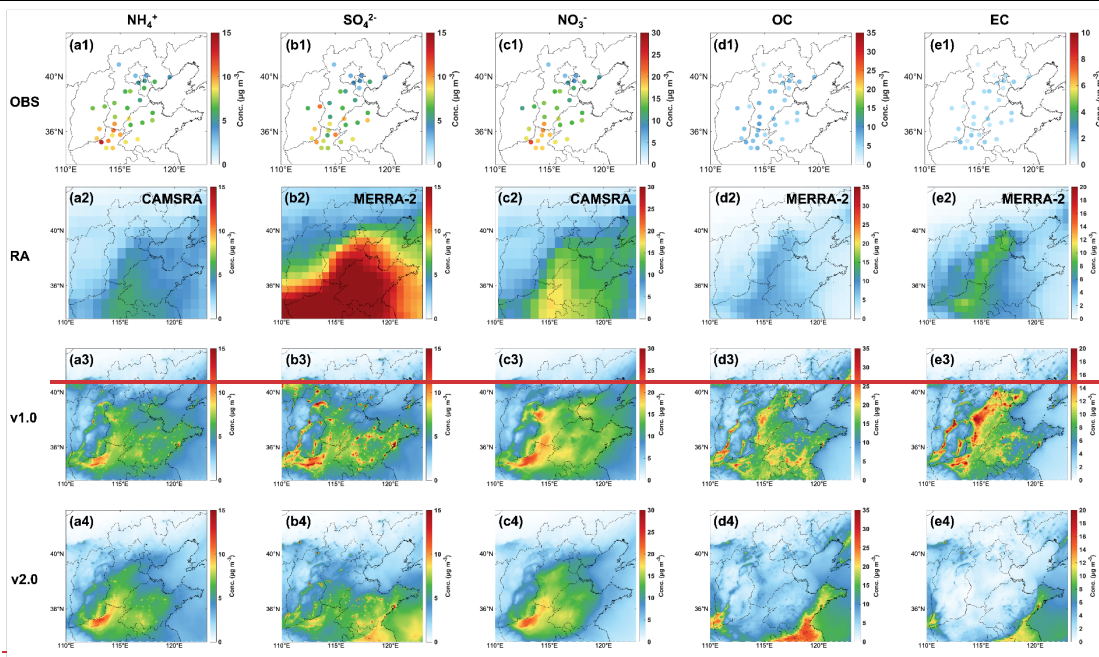
89
90 The spatial distributions of OC and EC exhibit similarities (Fig. 10d1 and e1), consistent with the finding of a strong correlation
91 between OC and EC in winter (Cao et al., 2007). Since the low temperature and weakened photochemical reactions in winter
92 reduced secondary OC (SOC) generation, and primary OC (POC) and EC mainly originate from direct anthropogenic
93 emissions, such as combustion (Guo, 2016). Compared to the OBS, the mass concentrations in FR (Fig. 10d2-d3) and FOR
94 (Fig. 10e2-e3) are significantly overestimated over a wide range. Similar overestimations have also been reported in the global
95 reanalysis datasets of CAMS and MERRA-2, likely attributed to the hygroscopic growth scheme of carbonaceous aerosols in
96 the models, poorly constrained semi-volatile species escaping from primary organic aerosols (Soni et al., 2021), and aging

97 mechanisms in the models (Huang et al., 2013). After DA, the spatial distribution of the ANA aligns entirely with that of the
98 OBS (Fig. 10d4 and e4), with the improvements in all overestimations (Fig. 10d5 and e5) and the average biases of OC and
99 EC at DA sites both significantly decreasing to $0.14 \mu\text{g}/\text{m}^3$ (Fig. 11d3 and e3). The VE sites show similar results to the DA
00 sites, with ~~the~~ average biases of less than $2 \mu\text{g}/\text{m}^3$ (Fig. S5d3 and e3). Specifically, for OC (Fig. 12d1 and d2), the CORR
01 values in FOR and ANA are 0.18-0.71 and 0.92-1.00, respectively, with RMSE values of $7.91 \mu\text{g}/\text{m}^3$ - $26.27 \mu\text{g}/\text{m}^3$ and 0.16
02 $\mu\text{g}/\text{m}^3$ - $1.45 \mu\text{g}/\text{m}^3$, respectively. For EC (Fig. 12e1 and e2), the CORR values in FOR and ANA are 0.01-0.66 and 0.97-1.00,
03 respectively, with RMSE values of $5.33 \mu\text{g}/\text{m}^3$ - $16.91 \mu\text{g}/\text{m}^3$ and $0.01 \mu\text{g}/\text{m}^3$ - $0.26 \mu\text{g}/\text{m}^3$, respectively. Although significant
04 improvements are not observed in FOR at some specific DA sites, the RMSE values at all DA sites decrease by 10%-50% (Fig.
05 12d3 and e3). The CORR values of OC and EC in ANA increase by more than 30%, with most DA sites exceeding 200%, and
06 the RMSE values decrease by more than 90% (Fig. 12d4 and e4). At VE sites (Fig. S6), significant improvements in the CORR
07 are not observed, but the RMSE values in the FOR and ANA decrease, which indicates that DA has limited benefits for whole
08 areas but can effectively reduce biases of ~~whole areas~~ entire regions.

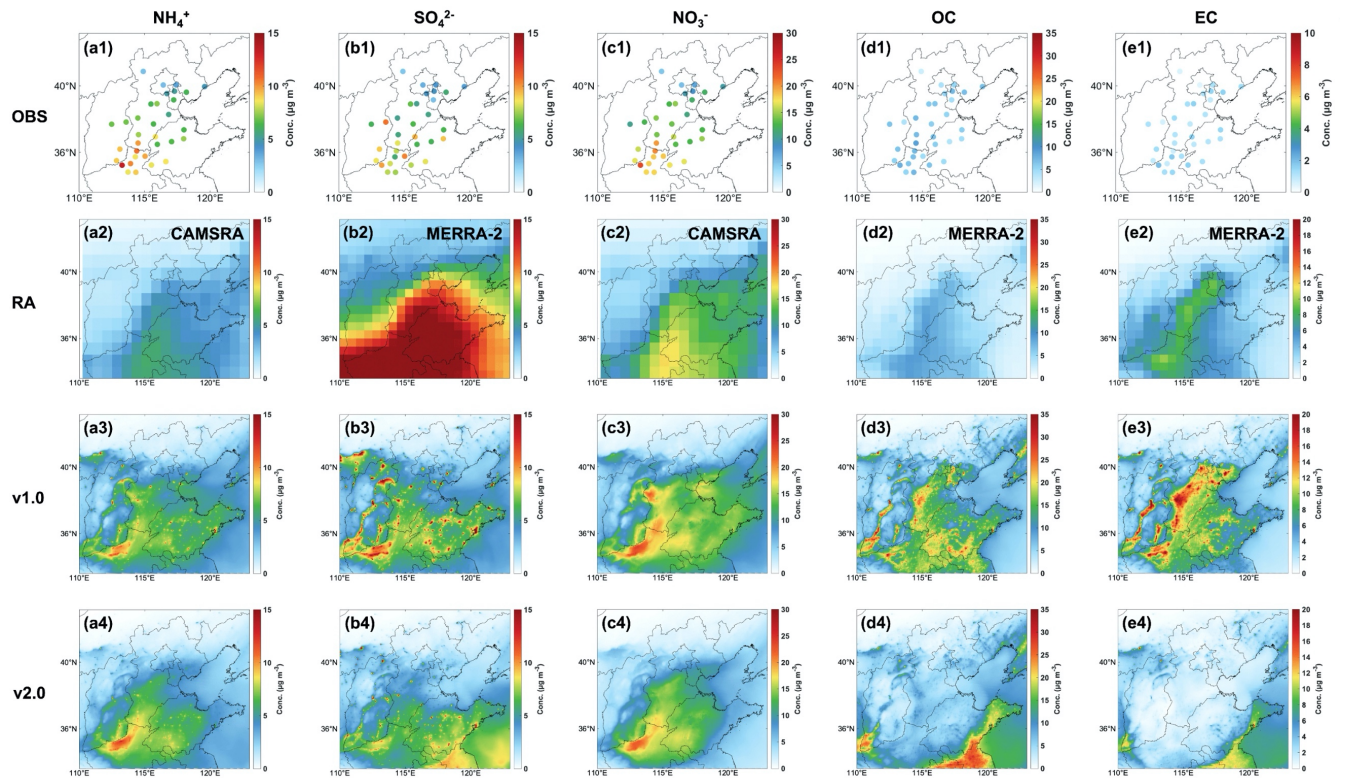
09 3.3 Compared to NAQPMS-PDAF v1.0 and global reanalysis dataset

10 To comprehensively evaluate the competitiveness and superiority of NAQPMS-PDAF v2.0 in generating the reanalysis
11 datasets of the $\text{PM}_{2.5}$ chemical compositions, we assimilated the mass concentrations of the five $\text{PM}_{2.5}$ chemical components
12 from all sites (sum of DA sites and VE sites) in February 2022 to generate a reanalysis dataset. We compared our reanalysis
13 dataset with the global reanalysis (RA) datasets (CAMSRA and MERRA-2) and NAQPMS-PDAF v1.0 output. Figure 13
14 illustrates the spatial distribution of the monthly average mass concentrations for the five chemical components. Compared to
15 the OBS (Fig. 13a1 and c1), CAMSRA underestimates the NH_4^+ and NO_3^- concentrations and fails to capture the high-value
16 concentration in northern Henan Province (Fig. 13a2 and c2). Meanwhile, MERRA-2 overestimates the concentrations of
17 SO_4^{2-} , OC, and EC (Fig. 13b2, d2, and e2), particularly SO_4^{2-} , exhibiting a large region with inaccurately high concentrations.
18 Besides, CAMSRA (approximately $80 \times 80 \text{ km}^2$) and MERRA-2 ($55 \times 70 \text{ km}^2$) have significantly lower spatial resolutions
19 compared to NAQPMS-PDAF v2.0 ($5 \times 5 \text{ km}^2$). Therefore, NAQPMS-PDAF v2.0 provides a more detailed description of the
20 pollution characteristics of chemical components in Northern China and surrounding areas compared to RA.

21



22



23 **Figure 13: Spatial distribution of the monthly averaged concentration of five PM_{2.5} chemical components for observations (OBS, a1-**
 24 **e1), global reanalysis data (RA, a2-e2), NAQPMS-PDAF v1.0 analysis data (a3-e3) and NAQPMS-PDAF v2.0 analysis data (a4-e4).**

25 Although NAQPMS-PDAF v1.0 demonstrates a superior spatial representation of the five chemical components when
 26 compared to RA, it fails to capture the high-value concentrations of NH₄⁺ in the northwest of Henan Province and correct the
 27 high-value concentrations of NH₄⁺ in the central and western areas of Hebei Province (Fig. 13a3). Moreover, the scattered
 28 high-value concentrations of SO₄²⁻ in the North China Plain do not align with the spatial characteristics of the OBS (Fig. 13b3).
 29 Notably, NAQPMS-PDAF v1.0 exhibits poor performance in interpreting OC and EC with significant overestimations in a

30 wide range (Fig. 13d3 and e3), which indicates that NAQPMS-PDAF v1.0 is weaker than NAQPMS-PDAF v2.0 in terms of
 31 DA performance on chemical components, primarily due to insufficient propagation of observations. In NAQPMS-PDAF v2.0,
 32 the LKNETF algorithm with an adaptive forgetting factor is more suitable for the nonlinear and non-Gaussian situations
 33 compared to EnKFs in NAQPMS-PDAF v1.0, and the ensemble perturbation with non-Gaussian distribution can better
 34 represent the reasonable error distribution of model states.

35
 36 Table 3 presents a quantitative comparison of three reanalysis datasets. Compared to the CORR of NAQPMS-PDAF v2.0
 37 (0.86-0.99), the CORR of RA for the five chemical components is significantly lower (0.42-0.55). Moreover, NAQPMS-PDAF
 38 v1.0 exhibits significantly poorer consistency in SO_4^{2-} , OC, and EC, with CORR values ranging from 0.35 to 0.57. NAQPMS-
 39 PDAF v2.0 has lower overall RMSE values ($0.14 \mu\text{g}/\text{m}^3$ - $3.18 \mu\text{g}/\text{m}^3$) compared to RA and NAQPMS-PDAF v1.0, with RMSE
 40 values ranging from $4.51 \mu\text{g}/\text{m}^3$ to $12.27 \mu\text{g}/\text{m}^3$ and $2.46 \mu\text{g}/\text{m}^3$ to $15.50 \mu\text{g}/\text{m}^3$, respectively. The characteristics of ~~the~~ R^2 are
 41 likesimilar to those of ~~the~~ CORR and RMSE. For NH_4^+ and NO_3^- , NAQPMS-PDAF v2.0 (0.85 and 0.93) and v1.0 (0.80 and
 42 0.96) are much higher than RA (0.09 and 0.13). Notably, for SO_4^{2-} , OC, and EC, NAQPMS-PDAF v2.0 (0.74-0.98) is
 43 significantly higher than v1.0 (-0.16-0.25) and RA (-0.15-0.25). Overall, NAQPMS-PDAF v2.0 more accurately and
 44 consistently interprets the five chemical components, particularly for NH_4^+ , SO_4^{2-} , OC, and EC. The reasons are summarized
 45 as follows. (1) The DA frequency of CAMSRA is 12 hours, which is lower than the hourly DA frequency in NAQPMS-PDAF
 46 v2.0. (2) CAMSRA only assimilates satellite retrievals (Inness et al., 2019), and MERRA-2 only assimilates aerosol optical
 47 depth (AOD) from both ground-based and space-based remote sensing platforms (Randles et al., 2017). The aerosol optical
 48 information analysis increment cannot be allocated to each chemical component accurately and reasonably due to the lack of
 49 a deterministic relationship between aerosol optical information and $\text{PM}_{2.5}$ chemical components. (3) NAQPMS-PDAF v1.0
 50 has evident DA shortcomings for chemical components due to the limited DA algorithm under the assumption of a linear model
 51 or system, inappropriate ensemble perturbation under the assumption of Gaussian distribution, and inadequate observational
 52 modules. (4) The state variable structure in NAQPMS-PDAF v1.0 ~~lacks the capacity to~~ cannot effectively mitigate the impact
 53 of spurious correlations between chemical component variables, even when using analytical localization.

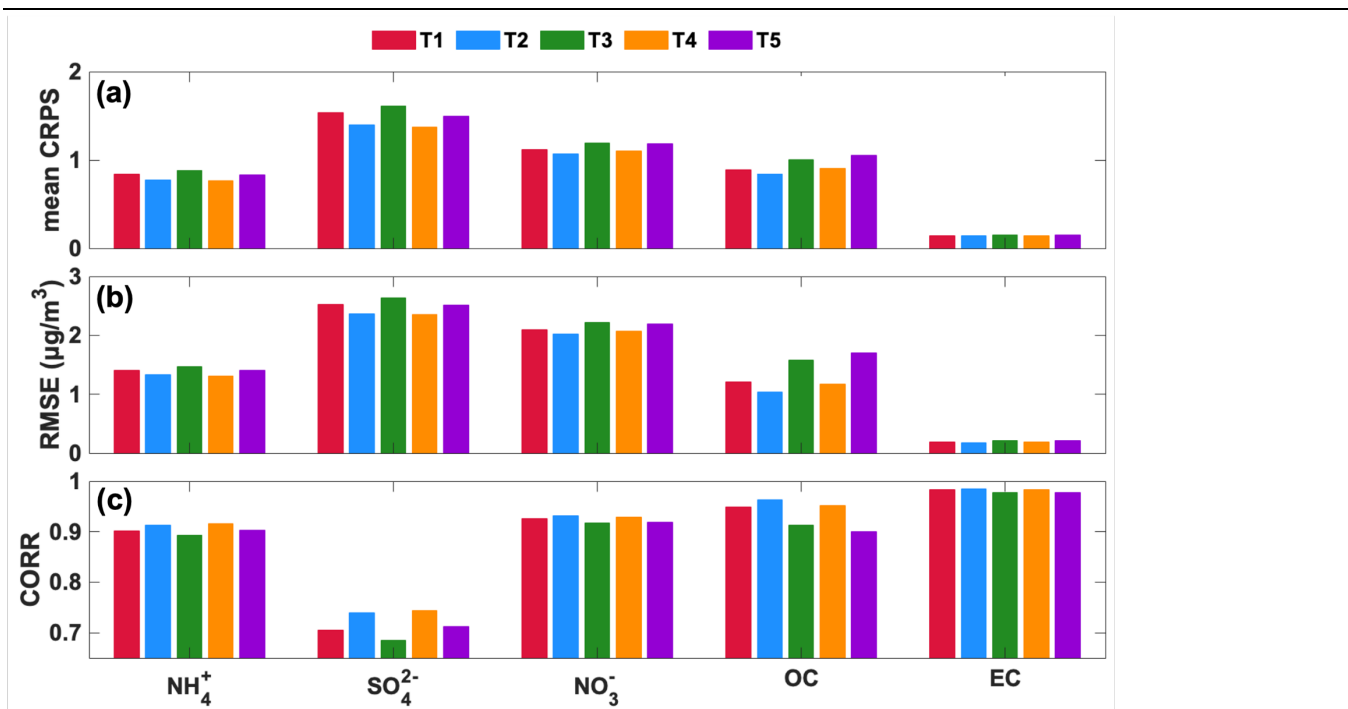
54 **Table 3: Statistical indicators (CORR, RMSE, R^2) of five $\text{PM}_{2.5}$ chemical components for global reanalysis data (RA), NAQPMS-
 55 PDAF v1.0 analysis data and NAQPMS-PDAF v2.0 analysis data.**

Components	CORR			RMSE ($\mu\text{g}/\text{m}^3$)			R^2		
	RA	v1.0	v2.0	RA	v1.0	v2.0	RA	v1.0	v2.0
NH_4^+	0.49	0.90	0.92	5.59	2.53	2.22	0.09	0.80	0.85
SO_4^{2-}	0.55	0.57	0.86	12.27	5.45	2.61	0.25	0.25	0.74
NO_3^-	0.54	0.98	0.96	10.27	2.46	3.18	0.13	0.96	0.93
OC	0.50	0.42	0.97	4.51	12.92	0.93	0.15	-0.09	0.93
EC	0.42	0.35	0.99	7.59	15.50	0.14	-0.15	-0.16	0.98

56 **3.4 The uncertainty in NAQPMS-PDAF v2.0**

57 In ensemble DA, the ensemble members represent possible values of the model states, and the ensemble sampling can
58 determine the uncertainties of the model states. Therefore, the ensemble generation directly affects the propagation of
59 observations and subsequently impacts the final DA performance. Previous studies generated ensemble members based on the
60 uncertainties of emission species and the Gaussian-distribution assumption to satisfy the requirements of EnKFs algorithms
61 (Kong et al., 2021; Wang et al., 2022). However, the true error probability distribution of emission species is not an ideal
62 Gaussian distribution, and the assumption will introduce errors. In this study, we coupled the hybrid nonlinear DA algorithm
63 (LKNETF) with NAQPMS to handle the nonlinear and non-Gaussian situations, which combines the stability of LETKF with
64 the nonlinearity of LNETF. Therefore, we evaluate the performance of ensemble members with different uncertainties and
65 error probability distributions in NAQPMS-PDAF v2.0 through two groups of sensitivity experiments.

66
67 The first group of experiments (T1-T5) involves controlling the SO₂ uncertainty as a fixed value of 200% and transforming
68 the distribution of the perturbation coefficient matrix. The second group of experiments (M1-M5) focuses on assessing the
69 influence of SO₂ uncertainty on NH₄⁺ and SO₄²⁻ DA based on a fixed non-Gaussian distribution (m3=1, m4=6). Figure 14
70 shows the statistical indicators of the five chemical components under different error probability distributions, including a
71 Gaussian distribution (T1) and four non-Gaussian distributions (T2-T5). The mean CRPS and RMSE in T2 and T4 are lower
72 than those in T1, T3, and T5, and the CORR values in T2 and T4 are higher than those in T1, T3, and T5, indicating that the
73 DA performance of non-Gaussian-distribution assumption is superior to that of Gaussian-distribution assumption. Moreover,
74 positively skewed non-Gaussian distribution performs better than negatively skewed distribution. Except for SO₄²⁻, the
75 performance in T2 outweighs that in T4 for other chemical components, implying that higher kurtosis harms the chemical
76 components DA.



77
78
79

Figure 14: Statistical indicators (mean CRPS (a), RMSE (b), and CORR (c)) of five PM_{2.5} chemical components for five perturb experiments based on distribution.

80

SO₂ is a crucial precursor of NH₄⁺ and SO₄²⁻, and perturbing SO₂ affects the forecast and simulation of NH₄⁺ and SO₄²⁻. Table 4 presents statistical indicators of NH₄⁺ and SO₄²⁻ analysis fields based on ensemble perturbations with different SO₂ uncertainties (12%-300%). Increasing the uncertainty of SO₂ from 12% to 200% leads to a decrease in the mean CRPS in the SO₄²⁻ analysis field from 2.67 to 1.40, an increase in the CORR from 0.51 to 0.74, and a reduction in the RMSE from 4.10 µg/m³ to 2.37 µg/m³. Similarly, the mean CRPS in the NH₄⁺ analysis field decreases from 0.98 to 0.77, the CORR increases from 0.88 to 0.91, and the RMSE decreases from 1.55 µg/m³ to 1.33 µg/m³. It indicates that increasing the uncertainty of SO₂ improves the DA performance on NH₄⁺ and SO₄²⁻ because the higher SO₂ uncertainty makes SO₂ perturbed sufficiently, and the estimated error probability distribution is closer to the real distribution, resulting in a sufficient spread of observations. However, when the uncertainty of SO₂ reaches 300%, the statistical indicators do not significantly improve and even worsen because excessively high SO₂ uncertainty causes the estimated error probability distribution to deviate from the true distribution. Thus, selecting appropriate uncertainties for emission species is crucial in aerosol chemical component DA.

91

92

To summarize, the non-Gaussian distribution assumption outperforms the Gaussian distribution assumption in NAQPMS-PDAF v2.0. Positive skewness performs better than negative skewness, and excessively high kurtosis should be avoided. Additionally, appropriately increasing the uncertainty of SO₂ enhances the DA performance of NH₄⁺ and SO₄²⁻. Future studies should conduct more sensitivity experiments on emission species perturbation to determine the suitable schemes for different aerosol chemical components.

96

97 **Table 4: Statistical indicators (mean CRPS (a), RMSE (b), and CORR (c)) of five PM_{2.5} chemical components for five perturb**
 98 **experiments based on SO₂ emission uncertainty.**

Experiment	SO ₄ ²⁻			NH ₄ ⁺		
	CRPS	CORR	RMSE	CRPS	CORR	RMSE
M1	2.67	0.51	4.10	0.98	0.88	1.55
M2	2.07	0.59	3.24	0.92	0.89	1.48
M3	1.61	0.69	2.63	0.83	0.91	1.39
M4	1.40	0.74	2.37	0.77	0.91	1.33
M5	1.41	0.74	2.39	0.78	0.91	1.33

99 **4 Conclusions**

00 In this paper, we online coupled NAQPMS with PDAF-OMI to develop a novel hybrid nonlinear DA system (NAQPMS-
 01 PDAF v2.0) with level-2 parallelization based on a hybrid Kalman-Nonlinear Ensemble Transform Filter (LKNETF) for the
 02 first time. Compared to NAQPMS-PDAF v1.0, NAQPMS-PDAF v2.0 with OMI can be applied with multiple component
 03 types and nonlinear/non-Gaussian situations in chemical analysis to effectively interpret five PM_{2.5} chemical components
 04 (NH₄⁺, SO₄²⁻, NO₃⁻, OC and EC), which is not achieved in previous studies. The background error covariance was calculated
 05 by ensemble perturbation based on adaptive uncertainties and non-Gaussian distribution assumption of emission species. The
 06 DA experiments were conducted based on 33 observational sites in Northern China and surrounding areas.

07
 08 NAQPMS-PDAF v2.0 with LKNETF can maintain high accuracy and reliability in ensemble DA with an ensemble size of 10,
 09 smaller than the traditional minimum of 20 ensemble members, as observed in prior ensemble assimilation studies. The FR
 10 (free-run fields without DA) have a poor consistency with the observations, with the CORR values ranging from 0.32-0.56
 11 and the R² values less than 0.3, showing that SO₄²⁻, OC and EC are significantly overestimated, while NH₄⁺ and NO₃⁻ are
 12 underestimated. A significant improvement was observed in the ANA (analysis fields) ~~of~~at the DA sites. The CORR values are
 13 not less than 0.86, the RMSE and MAE values do not exceed 3.23 μg/m³ and 1.49 μg/m³, respectively, and R² is not less than
 14 0.74. Specifically, the CORR values for NO₃⁻, OC, and EC are not less than 0.96, and R² is not less than 0.93. The error
 15 distributions of the five chemical components concentrate to 0 with the mean bias ranging from 0±0.08 μg/m³ to 1.02±3.07
 16 μg/m³. These improvements are also found in the ANA at VE sites, indicating an excellent DA performance of NAQPMS-
 17 PDAF v2.0.

18
 19 The ability of NAQPMS-PDAF v2.0 to interpret the spatiotemporal characteristics of the five chemical components was
 20 examined. For temporal variations, compared to the FR and FOR (forecast fields), the ANA closely aligned with the OBS
 21 (observations) and accurately captured the peak concentrations of SO₄²⁻, NO₃⁻, and NH₄⁺ on specific periods (such as February

22 25th), indicating good consistency and accurate characterization. Specifically, the CORR of the ANA at the six representative
23 sites increased by 13.64%-89.58% and 17.19%-75.00%, respectively, while the RMSE decreased by 56.03%-83.13% and
24 40.74%-72.20%. For spatial distributions, after DA, both NH_4^+ and NO_3^- with positive analysis increments exhibit significant
25 improvements in CORR and RMSE, as most DA sites show improvements of over 150% in CORR and over 50% in RMSE.
26 SO_4^{2-} , OC, and EC with negative analysis increments were also improved. Especially for OC and EC, the improvements of
27 CORR and RMSE at most DA sites were over 200% and over 90%, respectively. The improvements at VE sites were also
28 identified. Consequently, DA successfully aligned the spatiotemporal characteristics of the ANA with OBS and significantly
29 reduced the biases of five chemical components.

30
31 Compared to the global reanalysis datasets (CORR: 0.42-0.55, RMSE: 4.51-12.27 $\mu\text{g}/\text{m}^3$) and NAQPMS-PDAF v1.0 (CORR:
32 0.35-0.98, RMSE: 2.46-15.50 $\mu\text{g}/\text{m}^3$), the NAQPMS-PDAF v2.0 (CORR: 0.86-0.99, RMSE: 0.14-3.18 $\mu\text{g}/\text{m}^3$) has significant
33 superiority in generating the reanalysis datasets of the $\text{PM}_{2.5}$ chemical compositions with high spatiotemporal resolution.
34 Besides, NAQPMS-PDAF v1.0 cannot capture the high-value concentrations and exhibits poor performance when interpreting
35 SO_4^{2-} , OC, and EC with CORR values ranging from 0.35 to 0.57. In contrast, NAQPMS-PDAF v2.0 interprets the five chemical
36 components more accurately and consistently.

37
38 Finally, the uncertainties of NAQPMS-PDAF v2.0 are examined by identifying the influence of ensemble generation on
39 ensemble DA performance. The non-Gaussian-distribution assumption outperforms the Gaussian-distribution assumption in
40 NAQPMS-PDAF v2.0. Positive skewness performs better than negative skewness, and excessively high kurtosis should be
41 avoided. Additionally, appropriately increasing the uncertainty of SO_2 enhances the DA performance of NH_4^+ and SO_4^{2-} . Future
42 studies should conduct more sensitivity experiments on emission species perturbation to determine the suitable schemes for
43 different aerosol chemical components.

44
45 The novel hybrid nonlinear DA system (NAQPMS-PDAF v2.0) can be effectively applied in the interpretation of chemical
46 components and outperform in generating the reanalysis dataset of the five $\text{PM}_{2.5}$ chemical components with high accuracy
47 and high consistency, thus providing the sufficient channel to investigate the spatiotemporal characteristics, identify the
48 regional transport and prevent and control aerosol composition pollution. In future work, we plan to research the vertical DA
49 of chemical components, introduce more vertical information from more observational platforms, and verify the simultaneous
50 DA performance of surface and vertical mass concentrations.

51

52 **Code and data availability**

53 The source codes in our work are available online via Zenodo (<https://doi.org/10.5281/zenodo.10886914>).

54 **Author contributions**

55 HL developed the data assimilation system, performed numerical experiments, carried out the analysis, and wrote the original
56 manuscript. TY provided scientific guidance, designed the paper ~~structure~~, and wrote this paper. LN developed PDAF
57 and provided help for the model code. DWZ, DZ, and GT provided PM_{2.5} chemical component data. HW provided help ~~for~~with
58 the model code. YS, PF, HS, and ZW did overall supervision. All authors reviewed and revised this paper.

59 **Competing interests**

60 The contact author has declared that neither they nor their co-authors have any competing interests.

61 **Acknowledgements**

62 This work was supported by the National Key Research and Development Program for Young Scientists of China (No.
63 2022YFC3704000), the National Natural Science Foundation of China (No. 42275122), and the National Key Scientific and
64 Technological Infrastructure project “Earth System Science Numerical Simulator Facility” (EarthLab). Ting Yang would like
65 to express gratitude towards the Program of the Youth Innovation Promotion Association (CAS). We thank the Big Data Cloud
66 Service Infrastructure Platform (BDCSIP) for providing computing resources.
67

- 69 Aleksankina, K., Heal, M. R., Dore, A. J., Van Oijen, M., and Reis, S.: Global sensitivity and uncertainty analysis of an
70 atmospheric chemistry transport model: the FRAME model (version 9.15.0) as a case study, *Geosci. Model Dev.*, 11, 1653-
71 1664, <https://doi.org/10.5194/gmd-11-1653-2018>, 2018.
- 72 Ali, A., Amin, S. E., Ramadan, H. H., and Tolba, M. F.: Enhancement of OMI aerosol optical depth data assimilation using
73 artificial neural network, *Neural Computing and Applications*, 23, 2267-2279, <https://doi.org/10.1007/s00521-012-1178-9>,
74 2013.
- 75 Alves, C., Evtuygina, M., Vicente, E., Vicente, A., Rienda, I. C., de la Campa, A. S., Tomé, M., and Duarte, I.: PM_{2.5} chemical
76 composition and health risks by inhalation near a chemical complex, *J. Environ. Sci.*, 124, 860-874,
77 <https://doi.org/10.1016/j.jes.2022.02.013>, 2023.
- 78 Amante, C. and Eakins, B. W.: ETOPO1 arc-minute global relief model: procedures, data sources and analysis, 2009.
- 79 Arthur, D. and Vassilvitskii, S.: K-means++: the advantages of careful seeding, *Proceedings of the eighteenth annual ACM-
80 SIAM symposium on Discrete algorithms*, 1027-1035, <https://dl.acm.org/doi/10.5555/1283383.1283494>, 2007
- 81 Bao, Y., Zhu, L., Guan, Q., Guan, Y., Lu, Q., Petropoulos, G. P., Che, H., Ali, G., Dong, Y., Tang, Z., Gu, Y., Tang, W., and
82 Hou, Y.: Assessing the impact of Chinese FY-3/MERSI AOD data assimilation on air quality forecasts: Sand dust events in
83 northeast China, *Atmos. Environ.*, 205, 78-89, <https://doi.org/10.1016/j.atmosenv.2019.02.026>, 2019.
- 84 Bell, M. L., Dominici, F., Ebisu, K., Zeger, S. L., and Samet, J. M.: Spatial and temporal variation in PM_{2.5} chemical
85 composition in the United States for health effects studies, *Environ. Health Perspect.*, 115, 989-995,
86 <https://doi.org/10.1289/ehp.9621>, 2007.
- 87 Bishop, C. H., Etherton, B. J., and Majumdar, S. J.: Adaptive Sampling with the Ensemble Transform Kalman Filter. Part I:
88 Theoretical Aspects, *Mon. Weather Rev.*, 129, 420-436, [https://doi.org/10.1175/1520-
89 0493\(2001\)129<0420:ASWTET>2.0.CO;2](https://doi.org/10.1175/1520-0493(2001)129<0420:ASWTET>2.0.CO;2), 2001.
- 90 Cao, J. J., Lee, S. C., Chow, J. C., Watson, J. G., Ho, K. F., Zhang, R. J., Jin, Z. D., Shen, Z. X., Chen, G. C., Kang, Y. M., Zou,
91 S. C., Zhang, L. Z., Qi, S. H., Dai, M. H., Cheng, Y., and Hu, K.: Spatial and seasonal distributions of carbonaceous aerosols
92 over China, *J. Geophys Res.-Atmos.*, 112, <https://doi.org/10.1029/2006jd008205>, 2007.
- 93 Chai, T., Kim, H. C., Pan, L., Lee, P., and Tong, D.: Impact of moderate resolution imaging spectroradiometer aerosol optical
94 depth and airnow PM_{2.5} assimilation on community multi-scale air quality aerosol predictions over the contiguous United
95 States, *J. Geophys Res.*, 122, 5399-5415, <https://doi.org/10.1002/2016JD026295>, 2017.
- 96 Chang, W., Zhang, Y., Li, Z., Chen, J., and Li, K.: Improving the sectional Model for Simulating Aerosol Interactions and
97 Chemistry (MOSAIC) aerosols of the Weather Research and Forecasting-Chemistry (WRF-Chem) model with the revised
98 Gridpoint Statistical Interpolation system and multi-wavelength aerosol optical measurements: The dust aerosol observation
99 campaign at Kashi, near the Taklimakan Desert, northwestern China, *Atmos. Chem. Phys.*, 21, 4403-4430,
00 <https://doi.org/10.5194/acp-21-4403-2021>, 2021.
- 01 Chang, W., Liao, H., Xin, J., Li, Z., Li, D., and Zhang, X.: Uncertainties in anthropogenic aerosol concentrations and direct
02 radiative forcing induced by emission inventories in eastern China, *Atmos. Res.*, 166, 129-140,
03 <https://doi.org/10.1016/j.atmosres.2015.06.021>, 2015.
- 04 Cheng, Y., Dai, T., Goto, D., A J Schutgens, N., Shi, G., and Nakajima, T.: Investigating the assimilation of CALIPSO global
05 aerosol vertical observations using a four-dimensional ensemble Kalman filter, *Atmos. Chem. Phys.*, 19, 13445-13467,
06 <https://doi.org/10.5194/acp-19-13445-2019>, 2019.
- 07 [Cheynet, E.: Non-Gaussian process generation, https://github.com/ECheyne/Gaussian_to_nonGaussian/releases/tag/v1.2,](https://github.com/ECheyne/Gaussian_to_nonGaussian/releases/tag/v1.2)
08 [GitHub. Retrieved July 7, 2024.](#)
- 09 Constantinescu, E. M., Sandu, A., Chai, T., and Carmichael, G. R.: Assessment of ensemble-based chemical data assimilation
10 in an idealized setting, *Atmos. Environ.*, 41, 18-36, <https://doi.org/10.1016/j.atmosenv.2006.08.006>, 2007.
- 11 Dai, T., Schutgens, N. A. J., Goto, D., Shi, G., and Nakajima, T.: Improvement of aerosol optical properties modeling over
12 Eastern Asia with MODIS AOD assimilation in a global non-hydrostatic icosahedral aerosol transport model, *Environ. Pollut.*,

13 195, 319-329, <https://doi.org/10.1016/j.envpol.2014.06.021>, 2014.

14 Du, W., Dada, L., Zhao, J., Chen, X., Daellenbach, K. R., Xie, C., Wang, W., He, Y., Cai, J., Yao, L., Zhang, Y., Wang, Q., Xu,

15 W., Wang, Y., Tang, G., Cheng, X., Kokkonen, T. V., Zhou, W., Yan, C., Chu, B., Zha, Q., Hakala, S., Kurppa, M., Järvi, L.,

16 Liu, Y., Li, Z., Ge, M., Fu, P., Nie, W., Bianchi, F., Petäjä, T., Paasonen, P., Wang, Z., Worsnop, D. R., Kerminen, V.-M.,

17 Kulmala, M., and Sun, Y.: A 3D study on the amplification of regional haze and particle growth by local emissions, *npj Climate*

18 *and Atmospheric Science*, 4, 4, <https://doi.org/10.1038/s41612-020-00156-5>, 2021.

19 Evensen, G.: Sequential data assimilation with a nonlinear quasi-geostrophic model using Monte Carlo methods to forecast

20 error statistics, *J. Geophys Res.*, 99, <https://doi.org/10.1029/94jc00572>, 1994.

21 Evensen, G.: The Ensemble Kalman Filter: Theoretical formulation and practical implementation, *Ocean Dynamics*, 53, 343-

22 367, <https://doi.org/10.1007/s10236-003-0036-9>, 2003.

23 Friedman, J. H., Bentley, J. L., and Finkel, R. A.: An algorithm for finding best matches in logarithmic expected time, *ACM T.*

24 *Math. Software*, 3, 209-226, <https://doi.org/10.1145/355744.355745>, 1977.

25 Ge, B., Wang, Z., Xu, X., Wu, J., Yu, X., and Li, J.: Wet deposition of acidifying substances in different regions of China and

26 the rest of East Asia: Modeling with updated NAQPMS, *Environ. Pollut.*, 187, 10-21,

27 <https://doi.org/10.1016/j.envpol.2013.12.014>, 2014.

28 Ge, X., He, Y., Sun, Y., Xu, J., Wang, J., Shen, Y., and Chen, M.: Characteristics and Formation Mechanisms of Fine Particulate

29 Nitrate in Typical Urban Areas in China, *Atmosphere*, 8, <https://doi.org/10.3390/atmos8030062>, 2017.

30 Gordon, N. J., Salmond, D. J., and Smith, A. F.: Novel approach to nonlinear/non-Gaussian Bayesian state estimation, *IEE*

31 *Proc.-F*, 140, 107-113, <https://doi.org/10.1049/ip-f-2.1993.0015>, 1993.

32 Guo, Y.: Characteristics of size-segregated carbonaceous aerosols in the Beijing-Tianjin-Hebei region, *Environ. Sci. Pollut. R.*,

33 23, 13918-13930, <https://doi.org/10.1007/s11356-016-6538-z>, 2016.

34 Ha, S.: Implementation of aerosol data assimilation in WRFDA (v4.0.3) for WRF-Chem (v3.9.1) using the RACM/MADE-

35 VBS scheme, *Geosci. Model Dev.*, 15, 1769-1788, <https://doi.org/10.5194/gmd-15-1769-2022>, 2022.

36 Hamill, T. M. and Snyder, C.: A Hybrid Ensemble Kalman Filter-3D Variational Analysis Scheme, *Mon. Weather Rev.*, 128,

37 2905-2919, [https://doi.org/10.1175/1520-0493\(2000\)128<2905:AHEKfV>2.0.CO;2](https://doi.org/10.1175/1520-0493(2000)128<2905:AHEKfV>2.0.CO;2), 2000.

38 Hersbach, H.: Decomposition of the continuous ranked probability score for ensemble prediction systems, *Wea. Forecasting*,

39 15, 559-570, [https://doi.org/10.1175/1520-0434\(2000\)015<0559:DOTCRP>2.0.CO;2](https://doi.org/10.1175/1520-0434(2000)015<0559:DOTCRP>2.0.CO;2), 2000.

40 Horowitz, L. W., Walters, S., Mauzerall, D. L., Emmons, L. K., Rasch, P. J., Granier, C., Tie, X., Lamarque, J. F., Schultz, M.

41 G., Tyndall, G. S., Orlando, J. J., and Brasseur, G.P.: A global simulation of tropospheric ozone and related tracers: Description

42 and evaluation of MOZART, version 2, *J. Geophys Res.-Atmos.*, 108, <https://doi.org/10.1029/2002JD002853>, 2003.

43 Houtekamer, P. L. and Zhang, F.: Review of the Ensemble Kalman Filter for Atmospheric Data Assimilation, *Mon. Weather*

44 *Rev.*, 144, 4489-4532, <https://doi.org/10.1175/mwr-d-15-0440.1>, 2016.

45 Huang, B., Pagowski, M., Trahan, S., Martin, C. R., Tangborn, A., Kondragunta, S., and Kleist, D. T.: JEDI-Based Three-

46 Dimensional Ensemble-Variational Data Assimilation System for Global Aerosol Forecasting at NCEP, *J. Adv. Model. Earth*

47 *Sy.*, 15, <https://doi.org/10.1029/2022ms003232>, 2023.

48 Huang, Y., Wu, S., Dubey, M. K., and French, N. H. F.: Impact of aging mechanism on model simulated carbonaceous aerosols,

49 *Atmos. Chem. Phys.*, 13, 6329-6343, <https://doi.org/10.5194/acp-13-6329-2013>, 2013.

50 Huneus, N., Boucher, O., and Chevallier, F.: Atmospheric inversion of SO₂ and primary aerosol emissions for the year 2010,

51 *Atmos. Chem. Phys.*, 13, 6555-6573, <https://doi.org/10.5194/acp-13-6555-2013>, 2013.

52 Huneus, N., Chevallier, F., and Boucher, O.: Estimating aerosol emissions by assimilating observed aerosol optical depth in

53 a global aerosol model, *Atmos. Chem. Phys.*, 12, 4585-4606, <https://doi.org/10.5194/acp-12-4585-2012>, 2012.

54 Hunt, B. R., Kostelich, E. J., and Szunyogh, I.: Efficient data assimilation for spatiotemporal chaos: A local ensemble transform

55 Kalman filter, *Physica D*, 230, 112-126, <https://doi.org/10.1016/j.physd.2006.11.008>, 2007.

56 Inness, A., Ades, M., Agustí-Panareda, A., Barré, J., Benedictow, A., Blechschmidt, A. M., Dominguez, J. J., Engelen, R.,

57 Eskes, H., Flemming, J., Huijnen, V., Jones, L., Kipling, Z., Massart, S., Parrington, M., Peuch, V. H., Razinger, M., Remy, S.,

58 Schulz, M., and Suttie, M.: The CAMS reanalysis of atmospheric composition, *Atmos. Chem. Phys.*, 19, 3515-3556,

59 <https://doi.org/10.5194/acp-19-3515-2019>, 2019.

60 Jia, J., Cheng, S., Liu, L., Lang, J., Wang, G., Chen, G., and Liu, X.: An Integrated WRF-CAMx Modeling Approach for
61 Impact Analysis of Implementing the Emergency PM_{2.5} Control Measures during Red Alerts in Beijing in December 2015,
62 *Aerosol Air Qual. Res.*, 17, 2491-2508, <https://doi.org/10.4209/aaqr.2017.01.0009>, 2017.

63 Jin, J., Segers, A., Heemink, A., Yoshida, M., Han, W., and Lin, H. X.: Dust Emission Inversion Using Himawari-8 AODs
64 Over East Asia: An Extreme Dust Event in May 2017, *J. Adv. Model. Earth Sy.*, 11, 446-467,
65 <https://doi.org/10.1029/2018MS001491>, 2019.

66 Jolliffe, I. T. and Stephenson, D. B.: *Forecast verification: a practitioner's guide in atmospheric science*, John Wiley & Sons,
67 <https://doi.org/10.1002/9781119960003>, 2012.

68 Khanna, I., Khare, M., Gargava, P., and Khan, A. A.: Effect of PM_{2.5} chemical constituents on atmospheric visibility impairment,
69 *Journal of the Air & Waste Management Association*, 68, 430-437, <https://doi.org/10.1080/10962247.2018.1425772>, 2018.

70 Kim, G., Lee, S., Im, J., Song, C.-K., Kim, J., and Lee, M.-i.: Aerosol data assimilation and forecast using Geostationary Ocean
71 Color Imager aerosol optical depth and in-situ observations during the KORUS-AQ observing period, *GISci. Remote Sens.*,
72 58, 1175-1194, <https://doi.org/10.1080/15481603.2021.1972714>, 2021.

73 Kong, L., Tang, X., Zhu, J., Wang, Z., Li, J., Wu, H., Wu, Q., Chen, H., Zhu, L., Wang, W., Liu, B., Wang, Q., Chen, D., Pan,
74 Y., Song, T., Li, F., Zheng, H., Jia, G., Lu, M., Wu, L., and Carmichael, G. R.: A 6-year-long (2013–2018) high-resolution air
75 quality reanalysis dataset in China based on the assimilation of surface observations from CNEMC, *Earth Syst. Sci. Data*, 13,
76 529-570, <https://doi.org/10.5194/essd-13-529-2021>, 2021.

77 Kumar, R., Ghude, S. D., Biswas, M., Jena, C., Alessandrini, S., Debnath, S., Kulkarni, S., Sperati, S., Soni, V. K., Nanjundiah,
78 R. S., and Rajeevan, M.: Enhancing Accuracy of Air Quality and Temperature Forecasts During Paddy Crop Residue Burning
79 Season in Delhi Via Chemical Data Assimilation, *J. Geophys Res.-Atmos.*, 125, <https://doi.org/10.1029/2020JD033019>, 2020.

80 Kurtz, W., He, G., Kollet, S. J., Maxwell, R. M., Vereecken, H., and Hendricks Franssen, H. J.: TerrSysMP-PDAF (version
81 1.0): a modular high-performance data assimilation framework for an integrated land surface–subsurface model, *Geosci.*
82 *Model Dev.*, 9, 1341-1360, <https://doi.org/10.5194/gmd-9-1341-2016>, 2016.

83 Lawson, W. G. and Hansen, J. A.: Implications of Stochastic and Deterministic Filters as Ensemble-Based Data Assimilation
84 Methods in Varying Regimes of Error Growth, *Mon. Weather Rev.*, 132, 1966-1981, [https://doi.org/10.1175/1520-0493\(2004\)132<1966:IOSADF>2.0.CO;2](https://doi.org/10.1175/1520-0493(2004)132<1966:IOSADF>2.0.CO;2), 2004.

85

86 Li, H., Yang, T., Du, Y., Tan, Y., and Wang, Z.: [Interpreting hourly mass concentrations of PM_{2.5} chemical components with an
87 optimal deep-learning model. *J. Environ. Sci.*, 151, 125-139, <https://doi.org/10.1016/j.jes.2024.03.037>, 2025.](https://doi.org/10.1016/j.jes.2024.03.037)

88 Li, J., Li, X., Carlson, B. E., Kahn, R. A., Laci, A. A., Dubovik, O., and Nakajima, T.: Reducing multisensor satellite monthly
89 mean aerosol optical depth uncertainty: 1. Objective assessment of current AERONET locations, *J. Geophys Res.-Atmos.*, 121,
90 609-627, <https://doi.org/10.1002/2016JD025469>, 2016.

91 Li, J., Dong, Y., Song, Y., Dong, B., van Donkelaar, A., Martin, R. V., Shi, L., Ma, Y., Zou, Z., and Ma, J.: Long-term effects
92 of PM_{2.5} components on blood pressure and hypertension in Chinese children and adolescents, *Environ. Int.*, 161, 107134,
93 <https://doi.org/10.1016/j.envint.2022.107134>, 2022a.

94 Li, S., Chen, L., Huang, G., Lin, J., Yan, Y., Ni, R., Huo, Y., Wang, J., Liu, M., Weng, H., Wang, Y., and Wang, Z.: Retrieval
95 of surface PM_{2.5} mass concentrations over North China using visibility measurements and GEOS-Chem simulations, *Atmos.*
96 *Environ.*, 222, <https://doi.org/10.1016/j.atmosenv.2019.117121>, 2020.

97 Li, Y., Wang, X., Li, J., Zhu, L., and Chen, Y.: Numerical Simulation of Topography Impact on Transport and Source
98 Apportionment on PM_{2.5} in a Polluted City in Fenwei Plain, *Atmosphere*, 13, 233, <https://doi.org/10.3390/atmos13020233>,
99 2022b.

00 Lin, G. Y., Chen, H. W., Chen, B. J., and Chen, S. C.: A machine learning model for predicting PM_{2.5} and nitrate concentrations
01 based on long-term water-soluble inorganic salts datasets at a road site station, *Chemosphere*, 289,
02 <https://doi.org/10.1016/j.chemosphere.2021.133123>, 2022.

03 Liu, Y., Liu, J., Li, C., Yu, F., and Wang, W.: Effect of the Assimilation Frequency of Radar Reflectivity on Rain Storm
04 Prediction by Using WRF-3DVAR, *Remote Sens.*, 13, <https://doi.org/10.3390/rs13112103>, 2021.

05 Lloyd, S.: Least squares quantization in PCM, *IEEE T. Inform. Theory*, 28, 129-137, <https://doi.org/10.1109/TIT.1982.1056489>,
06 1982.

07 Luo, X., Liu, X., Pan, Y., Wen, Z., Xu, W., Zhang, L., Kou, C., Lv, J., and Goulding, K.: Atmospheric reactive nitrogen
08 concentration and deposition trends from 2011 to 2018 at an urban site in north China, *Atmos. Environ.*, 224,
09 <https://doi.org/10.1016/j.atmosenv.2020.117298>, 2020.

10 Lv, Z., Wei, W., Cheng, S., Han, X., and Wang, X.: Meteorological characteristics within boundary layer and its influence on
11 PM_{2.5} pollution in six cities of North China based on WRF-Chem, *Atmos. Environ.*, 228,
12 <https://doi.org/10.1016/j.atmosenv.2020.117417>, 2020.

13 Lynch, P., Reid, J. S., Westphal, D. L., Zhang, J., Hogan, T. F., Hyer, E. J., Curtis, C. A., Hegg, D. A., Shi, Y., Campbell, J. R.,
14 Rubin, J. I., Sessions, W. R., Turk, F. J., and Walker, A. L.: An 11-year global gridded aerosol optical thickness reanalysis (v1.0)
15 for atmospheric and climate sciences, *Geosci. Model Dev.*, 9, 1489-1522, <https://doi.org/10.5194/gmd-9-1489-2016>, 2016.

16 Mallet, V. and Sportisse, B.: Uncertainty in a chemistry-transport model due to physical parameterizations and numerical
17 approximations: An ensemble approach applied to ozone modeling, *J. Geophys. Res.-Atmos.*, 111,
18 <https://doi.org/10.1029/2005jd006149>, 2006.

19 Miao, R., Chen, Q., Zheng, Y., Cheng, X., Sun, Y., Palmer, P. I., Shrivastava, M., Guo, J., Zhang, Q., Liu, Y., Tan, Z., Ma, X.,
20 Chen, S., Zeng, L., Lu, K., and Zhang, Y.: Model bias in simulating major chemical components of PM_{2.5} in China, *Atmos.*
21 *Chem. Phys.*, 20, 12265-12284, <https://doi.org/10.5194/acp-20-12265-2020>, 2020.

22 Ming, L., Jin, L., Li, J., Fu, P., Yang, W., Liu, D., Zhang, G., Wang, Z., and Li, X.-E.-p.: PM_{2.5} in the Yangtze River Delta,
23 China: Chemical compositions, seasonal variations, and regional pollution events, 223, 200-212, 2017.

24 Mingari, L., Folch, A., Prata, A. T., Pardini, F., Macedonio, G., and Costa, A.: Data assimilation of volcanic aerosol
25 observations using FALL3D+PDAF, *Atmos. Chem. Phys.*, 22, 1773-1792, <https://doi.org/10.5194/acp-22-1773-2022>, 2022.

26 Miyazaki, K., Eskes, H. J., Sudo, K., Takigawa, M., van Weele, M., and Boersma, K. F.: Simultaneous assimilation of satellite
27 NO₂, O₃, CO, and HNO₃ data for the analysis of tropospheric chemical composition and emissions, *Atmos. Chem. Phys.*, 12,
28 9545-9579, <https://doi.org/10.5194/acp-12-9545-2012>, 2012.

29 Nerger, L.: On Serial Observation Processing in Localized Ensemble Kalman Filters, *Mon. Weather Rev.*, 143, 1554-1567,
30 <https://doi.org/10.1175/mwr-d-14-00182.1>, 2015.

31 Nerger, L.: Data assimilation for nonlinear systems with a hybrid nonlinear Kalman ensemble transform filter, *Q. J. Roy.*
32 *Meteor. Soc.*, 148, 620-640, <https://doi.org/10.1002/qj.4221>, 2022.

33 Nerger, L., Tang, Q., and Mu, L.: Efficient ensemble data assimilation for coupled models with the Parallel Data Assimilation
34 Framework: example of AWI-CM (AWI-CM-PDAF 1.0), *Geosci. Model Dev.*, 13, 4305-4321, <https://doi.org/10.5194/gmd-13-4305-2020>, 2020.

35
36 Nerger, L., Janjić, T., Schröter, J., and Hiller, W.: A Unification of Ensemble Square Root Kalman Filters, *Mon. Weather Rev.*,
37 140, 2335-2345, <https://doi.org/10.1175/mwr-d-11-00102.1>, 2012.

38 Nishizawa, T., Sugimoto, N., Matsui, I., Shimizu, A., and Okamoto, H.: Algorithms to retrieve optical properties of three
39 component aerosols from two-wavelength backscatter and one-wavelength polarization lidar measurements considering
40 nonsphericity of dust, *J. Quant. Spectrosc. Ra.*, 112, 254-267, <https://doi.org/10.1016/j.jqsrt.2010.06.002>, 2011.

41 Nishizawa, T., Okamoto, H., Takemura, T., Sugimoto, N., Matsui, I., and Shimizu, A.: Aerosol retrieval from two-wavelength
42 backscatter and one-wavelength polarization lidar measurement taken during the MR01K02 cruise of the R/V Mirai and
43 evaluation of a global aerosol transport model, *J. Geophys. Res.-Atmos.*, 113, <https://doi.org/10.1029/2007jd009640>, 2008.

44 Nishizawa, T., Sugimoto, N., Matsui, I., Shimizu, A., Hara, Y., Itsushi, U., Yasunaga, K., Kudo, R., and Kim, S. W.: Ground-
45 based network observation using Mie-Raman lidars and multi-wavelength Raman lidars and algorithm to retrieve distributions
46 of aerosol components, *J. Quant. Spectrosc. Ra.*, 188, 79-93, <https://doi.org/10.1016/j.jqsrt.2016.06.031>, 2017.

47 Park, R. S., Lee, S., Shin, S. K., and Song, C. H.: Contribution of ammonium nitrate to aerosol optical depth and direct radiative
48 forcing by aerosols over East Asia, *Atmos. Chem. Phys.*, 14, 2185-2201, <https://doi.org/10.5194/acp-14-2185-2014>, 2014.

49 Randles, C. A., da Silva, A. M., Buchard, V., Colarco, P. R., Darmenov, A., Govindaraju, R., Smirnov, A., Holben, B., Ferrare,
50 R., Hair, J., Shinozuka, Y., and Flynn, C. J.: The MERRA-2 aerosol reanalysis, 1980 onward. Part I: System description and

51 data assimilation evaluation, *J. Climate*, 30, 6823-6850, <https://doi.org/10.1175/JCLI-D-16-0609.1>, 2017.

52 Rodriguez, M. A., Brouwer, J., Samuelsen, G. S., and Dabdub, D.: Air quality impacts of distributed power generation in the
53 South Coast Air Basin of California 2: Model uncertainty and sensitivity analysis, *Atmos. Environ.*, 41, 5618-5635,
54 <https://doi.org/10.1016/j.atmosenv.2007.02.049>, 2007.

55 Rubin, J. I. and Collins, W. D.: Global simulations of aerosol amount and size using MODIS observations assimilated with an
56 Ensemble Kalman Filter, *J. Geophys Res. Atmospheres*, 119, 12,780-712,806, <https://doi.org/10.1002/2014JD021627>, 2014.

57 Rubin, J. I., Reid, J. S., Hansen, J. A., Anderson, J. L., Holben, B. N., Xian, P., Westphal, D. L., and Zhang, J. L.: Assimilation
58 of AERONET and MODIS AOT observations using variational and ensemble data assimilation methods and its impact on
59 aerosol forecasting skill, *J. Geophys Res.-Atmospheres*, 122, 4967-4992, <https://doi.org/10.1002/2016jd026067>, 2017.

60 Saide, P. E., Kim, J., Song, C. H., Choi, M., Cheng, Y., and Carmichael, G. R.: Assimilation of next generation geostationary
61 aerosol optical depth retrievals to improve air quality simulations, *Geophys. Res. Lett.*, 41, 9188-9196,
62 <https://doi.org/10.1002/2014GL062089>, 2014.

63 Sax, T. and Isakov, V.: A case study for assessing uncertainty in local-scale regulatory air quality modeling applications, *Atmos.*
64 *Environ.*, 37, 3481-3489, [https://doi.org/10.1016/S1352-2310\(03\)00411-4](https://doi.org/10.1016/S1352-2310(03)00411-4), 2003.

65 Schlesinger, R. B.: The health impact of common inorganic components of fine particulate matter (PM_{2.5}) in ambient air: a
66 critical review, *Inhal. Toxicol.*, 19, 811-832, <https://doi.org/10.1080/08958370701402382>, 2007.

67 Schult, I., Feichter, J., and Cooke, W. F.: Effect of black carbon and sulfate aerosols on the Global Radiation Budget, *J. Geophys*
68 *Res.-Atmospheres*, 102, 30107-30117, <https://doi.org/10.1029/97jd01863>, 1997.

69 Schutgens, N. A. J., Miyoshi, T., Takemura, T., and Nakajima, T.: Applying an ensemble Kalman filter to the assimilation of
70 AERONET observations in a global aerosol transport model, *Atmos. Chem. Phys.*, 10, 2561-2576, [https://doi.org/10.5194/acp-](https://doi.org/10.5194/acp-10-2561-2010)
71 [10-2561-2010](https://doi.org/10.5194/acp-10-2561-2010), 2010.

72 Schwartz, C. S., Liu, Z., Lin, H.-C., and Cetola, J. D.: Assimilating aerosol observations with a "hybrid" variational-ensemble
73 data assimilation system, *J. Geophys Res.-Atmospheres*, 119, 4043-4069, <https://doi.org/10.1002/2013jd020937>, 2014.

74 Soni, A., Mandariya, A. K., Rajeev, P., Izhar, S., Singh, G. K., Choudhary, V., Qadri, A. M., Gupta, A. D., Singh, A. K., and
75 Gupta, T.: Multiple site ground-based evaluation of carbonaceous aerosol mass concentrations retrieved from CAMS and
76 MERRA-2 over the Indo-Gangetic Plain, *Environm. Sci.-Atmos.*, 1, 577-590, <https://doi.org/10.1039/d1ea00067e>, 2021.

77 Strebel, L., Bogena, H. R., Vereecken, H., and Hendricks Franssen, H. J.: Coupling the Community Land Model version 5.0
78 to the parallel data assimilation framework PDAF: description and applications, *Geosci. Model Dev.*, 15, 395-411,
79 <https://doi.org/10.5194/gmd-15-395-2022>, 2022.

80 Su Lee, Y., Choi, E., Park, M., Jo, H., Park, M., Nam, E., Gon Kim, D., Yi, S.-M., and Young Kim, J.: Feature Extraction and
81 Prediction of Fine Particulate Matter (PM_{2.5}) Chemical Constituents using Four Machine Learning Models, *Expert Syst. Appl.*,
82 119696, <https://doi.org/10.1016/j.eswa.2023.119696>, 2023.

83 Talagrand, O. and Courtier, P.: Variational Assimilation of Meteorological Observations With the Adjoint Vorticity Equation.
84 I: Theory, *Q. J. Roy. Meteor. Soc.*, 113, 1311-1328, <https://doi.org/10.1002/qj.49711347812>, 1987.

85 Tang, Y., Chai, T., Pan, L., Lee, P., Tong, D., Kim, H. C., and Chen, W.: Using optimal interpolation to assimilate surface
86 measurements and satellite AOD for ozone and PM_{2.5}: A case study for July 2011, *Journal of the Air and Waste Management*
87 *Association*, 65, 1206-1216, <https://doi.org/10.1080/10962247.2015.1062439>, 2015.

88 Tippett, M. K., Anderson, J. L., Bishop, C. H., Hamill, T. M., and Whitaker, J. S.: Ensemble Square Root Filters, *Mon. Weather*
89 *Rev.*, 131, 1485-1490, [https://doi.org/10.1175/1520-0493\(2003\)131<1485:ESRF>2.0.CO;2](https://doi.org/10.1175/1520-0493(2003)131<1485:ESRF>2.0.CO;2), 2003.

90 Tödter, J. and Ahrens, B.: A Second-Order Exact Ensemble Square Root Filter for Nonlinear Data Assimilation, *Mon. Weather*
91 *Rev.*, 143, 1347-1367, <https://doi.org/10.1175/MWR-D-14-00108.1>, 2015.

92 Tödter, J., Kirchgessner, P., Nerger, L., and Ahrens, B.: Assessment of a Nonlinear Ensemble Transform Filter for High-
93 Dimensional Data Assimilation, *Mon. Weather Rev.*, 144, 409-427, <https://doi.org/10.1175/MWR-D-15-0073.1>, 2016.

94 Tsikerdekis, A., Schutgens, N. A. J., and Hasekamp, O. P.: Assimilating aerosol optical properties related to size and absorption
95 from POLDER/PARASOL with an ensemble data assimilation system, *Atmos. Chem. Phys.*, 21, 2637-2674,
96 <https://doi.org/10.5194/acp-21-2637-2021>, 2021.

97 Wang, H., Yang, T., Wang, Z., Li, J., Chai, W., Tang, G., Kong, L., and Chen, X.: An aerosol vertical data assimilation system
98 (NAQPMS-PDAF v1.0): development and application, *Geosci. Model Dev.*, 15, 3555-3585, [https://doi.org/10.5194/gmd-15-](https://doi.org/10.5194/gmd-15-3555-2022)
99 [3555-2022](https://doi.org/10.5194/gmd-15-3555-2022), 2022.

100 Wang, N., H. Guo, Jiang, F., Ling, Z. H., and Wang, T.: Simulation of ozone formation at different elevations in mountainous
101 area of Hong Kong using WRF-CMAQ model, *Sci. Total Environ.*, 505, 939-951,
102 <https://doi.org/10.1016/j.scitotenv.2014.10.070>, 2015.

103 Wang, T., Liu, H., Li, J., Wang, S., Kim, Y., Sun, Y., Yang, W., Du, H., Wang, Z., and Wang, Z.: A two-way coupled regional
104 urban–street network air quality model system for Beijing, China, *Geosci. Model Dev.*, 16, 5585-5599,
105 <https://doi.org/10.5194/gmd-16-5585-2023>, 2023.

106 Wang, Z., Itahashi, S., Uno, I., Pan, X., Osada, K., Yamamoto, S., Nishizawa, T., Tamura, K., and Wang, Z.: Modeling the
107 Long-Range Transport of Particulate Matters for January in East Asia using NAQPMS and CMAQ, *Aerosol Air Qual. Res.*,
108 17, 3065-3078, <https://doi.org/10.4209/aaqr.2016.12.0534>, 2017.

109 Wang, Z., Li, J., Wang, Z., Yang, W., Tang, X., Ge, B., Yan, P., Zhu, L., Chen, X., Chen, H., Wand, W., Li, J., Liu, B., Wang,
110 X., Wand, W., Zhao, Y., Lu, N., and Su, D.: Modeling study of regional severe hazes over mid-eastern China in January 2013
111 and its implications on pollution prevention and control, *Sci. China Earth Sci.*, 57, 3-13, [https://doi.org/10.1007/s11430-013-](https://doi.org/10.1007/s11430-013-4793-0)
112 [4793-0](https://doi.org/10.1007/s11430-013-4793-0), 2014. ~~Uno, I., Yumimoto, K., Pan, X., Chen, X., Li, J., Wang, Z., Shimizu, A., and Sugimoto, N.: Dust Heterogeneous~~
113 ~~Reactions during Long Range Transport of a Severe Dust Storm in May 2017 over East Asia, *Atmosphere*, 10, 680,~~
114 ~~<https://doi.org/10.3390/atmos10110680>, 2019.~~

115 ~~[Wang, Z., Maeda, T., Hayashi, M., Hsiao, L. F., and Liu, K. Y.: A Nested Air Quality Prediction Modeling System for Urban](https://doi.org/10.1023/A:1013833217916)~~
116 ~~[and Regional Scales: Application for High-Ozone Episode in Taiwan, *Water Air Soil Poll.*, 130, 391-396,](https://doi.org/10.1023/A:1013833217916)~~
117 ~~<https://doi.org/10.1023/A:1013833217916>, 2001.~~

118 ~~[Wang, Z., Uno, I., Yumimoto, K., Pan, X., Chen, X., Li, J., Wang, Z., Shimizu, A., and Sugimoto, N.: Dust Heterogeneous](https://doi.org/10.3390/atmos10110680)~~
119 ~~[Reactions during Long-Range Transport of a Severe Dust Storm in May 2017 over East Asia, *Atmosphere*, 10, 680,](https://doi.org/10.3390/atmos10110680)~~
120 ~~<https://doi.org/10.3390/atmos10110680>, 2019.~~ Wang, Z.,
121 ~~[Li, J., Wang, Z., Yang, W., Tang, X., Ge, B., Yan, P., Zhu, L., Chen, X., Chen, H., Wand, W., Li, J., Liu, B., Wang, X., Wand,](https://doi.org/10.1007/s11430-013-4793-0)~~
122 ~~[W., Zhao, Y., Lu, N., and Su, D.: Modeling study of regional severe hazes over mid-eastern China in January 2013 and its](https://doi.org/10.1007/s11430-013-4793-0)~~
123 ~~[implications on pollution prevention and control, *Sci. China Earth Sci.*, 57, 3-13, <https://doi.org/10.1007/s11430-013-4793-0>,](https://doi.org/10.1007/s11430-013-4793-0)~~
124 ~~[2014.](https://doi.org/10.1007/s11430-013-4793-0)~~

125 Werner, M., Kryza, M., and Guzikowski, J.: Can Data Assimilation of Surface PM_{2.5} and Satellite AOD Improve WRF-Chem
126 Forecasting? A Case Study for Two Scenarios of Particulate Air Pollution Episodes in Poland, *Remote Sens.*, 11,
127 <https://doi.org/10.3390/rs11202364>, 2019.

128 Wilcox, E. M., Thomas, R. M., Praveen, P. S., Pistone, K., Bender, F. A., and Ramanathan, V.: Black carbon solar absorption
129 suppresses turbulence in the atmospheric boundary layer, *P. Natl. Acad. Sci. USA*, 113, 11794-11799,
130 <https://doi.org/10.1073/pnas.1525746113>, 2016.

131 Xia, X., Min, J., Wang, Y., Shen, F., Yang, C., and Sun, Z.: Assimilating Himawari-8 AHI aerosol observations with a rapid-
132 update data assimilation system, *Atmos. Environ.*, 215, <https://doi.org/10.1016/j.atmosenv.2019.116866>, 2019.

133 Xia, X., Min, J., Shen, F., Wang, Y., Xu, D., Yang, C., and Zhang, P.: Aerosol data assimilation using data from Fengyun-4A,
134 a next-generation geostationary meteorological satellite, *Atmos. Environ.*, 237,
135 <https://doi.org/10.1016/j.atmosenv.2020.117695>, 2020.

136 Xie, X., Hu, J., Qin, M., Guo, S., Hu, M., Wang, H., Lou, S., Li, J., Sun, J., Li, X., Sheng, L., Zhu, J., Chen, G., Yin, J., Fu, W.,
137 Huang, C., and Zhang, Y.: Modeling particulate nitrate in China: Current findings and future directions, *Environ. Int.*, 166,
138 107369, <https://doi.org/10.1016/j.envint.2022.107369>, 2022.

139 Yan, Y., Zhou, Y., Kong, S., Lin, J., Wu, J., Zheng, H., Zhang, Z., Song, A., Bai, Y., Ling, Z., Liu, D., and Zhao, T.: Effectiveness
140 of emission control in reducing PM_{2.5} pollution in central China during winter haze episodes under various potential synoptic
141 controls, *Atmos. Chem. Phys.*, 21, 3143-3162, <https://doi.org/10.5194/acp-21-3143-2021>, 2021.

142 Yang, T., Li, H., Wang, H., Sun, Y., Chen, X., Wang, F., Xu, L., and Wang, Z.: Vertical aerosol data assimilation technology

43 and application based on satellite and ground lidar: A review and outlook, *J. Environ. Sci.*, 123, 292-305,
44 <https://doi.org/10.1016/j.jes.2022.04.012>, 2023.

45 Yang, X., Wu, Q., Zhao, R., Cheng, H., He, H., Ma, Q., Wang, L., and Luo, H.: New method for evaluating winter air quality:
46 PM_{2.5} assessment using Community Multi-Scale Air Quality Modeling (CMAQ) in Xi'an, *Atmos. Environ.*, 211, 18-28,
47 <https://doi.org/10.1016/j.atmosenv.2019.04.019>, 2019.

48 Ye, Q., Li, J., Chen, X., Chen, H., Yang, W., Du, H., Pan, X., Tang, X., Wang, W., Zhu, L., Li, J., Wang, Z., and Wang, Z.:
49 High-resolution modeling of the distribution of surface air pollutants and their intercontinental transport by a global
50 tropospheric atmospheric chemistry source-receptor model (GNAQPMS-SM), *Geosci. Model Dev.*, 14, 7573-7604,
51 <https://doi.org/10.5194/gmd-14-7573-2021>, 2021.

52 Yu, H. C., Zhang, Y. J., Nerger, L., Lemmen, C., Yu, J. C. S., Chou, T. Y., Chu, C. H., and Terng, C. T.: Development of a
53 flexible data assimilation method in a 3D unstructured-grid ocean model under Earth System Modeling Framework,
54 *EGUsphere* [preprint], 2022, 1-29, <https://doi.org/10.5194/egusphere-2022-114>, 2022.

55 Zhai, S. X., Jacob, D. J., Wang, X., Shen, L., Li, K., Zhang, Y. Z., Gui, K., Zhao, T. L., and Liao, H.: Fine particulate matter
56 (PM_{2.5}) trends in China, 2013-2018: separating contributions from anthropogenic emissions and meteorology, *Atmos. Chem.*
57 *Phys.*, 19, 11031-11041, <https://doi.org/10.5194/acp-19-11031-2019>, 2019.

58 Zhang, F., Wang, Z.-w., Cheng, H.-r., Lv, X.-p., Gong, W., Wang, X.-m., and Zhang, G.: Seasonal variations and chemical
59 characteristics of PM_{2.5} in Wuhan, central China, *Sci. Total Environ.*, 518-519, 97-105,
60 <https://doi.org/10.1016/j.scitotenv.2015.02.054>, 2015.

61 Zhang, J., Reid, J. S., Westphal, D. L., Baker, N. L., and Hyer, E. J.: A system for operational aerosol optical depth data
62 assimilation over global oceans, *J. Geophys Res.*, 113, <https://doi.org/10.1029/2007jd009065>, 2008.

63 Zhang, J., Campbell, J. R., Hyer, E. J., Reid, J. S., Westphal, D. L., and Johnson, R. S.: Evaluating the impact of multisensor
64 data assimilation on a global aerosol particle transport model, *J. Geophys Res.-Atmos.*, 119, 4674-4689,
65 <https://doi.org/10.1002/2013jd020975>, 2014.

66